Measurement of the Energy Relaxation Time in rf SQUID Flux Qubits

By

Wei Qiu

B.S., Beijing Polytechnic University, 1996

Submitted to the graduate program in Physics, and to the Graduate Faculty of the University of Kansas in partial fulfillment of the requirements for the degree of Doctor of Philosophy.

Chairperson _____
Dr. Siyuan Han (Dissertation Advisor)
Professor, Physics

Committee members _____
Dr. Judy Wu
University Distinguished Professor, Physics

_____
Dr. Philip S. Baringer
Professor, Physics

_____
Dr. Hui Zhao
Assistant Professor, Physics

_____
Dr. Shih-I Chu
Watkins Distinguished Professor, Chemistry

Date defended _____

The Dissertation Committee for Wei Qiu certifies that this is
the approved version of the following dissertation:

Measurement of the Energy Relaxation Time in rf SQUID Flux Qubits

Committee:

_____

_____

_____

_____

_____

Date approved _____

Abstract of the Dissertation

Measurement of the Energy Relaxation Time in rf SQUID Flux Qubits

Wei Qiu

Department of Physics and Astronomy

The University of Kansas, Lawrence, KS

September 2007

It is well known that that superconducting qubits based on Josephson junctions have the advantages of scalability and the qubit states are easy to prepare and control. In addition, demonstration of Rabi oscillations in various superconducting circuits shows that superconducting qubits are promising for scalable quantum information processing. However, despite flexibility of design and fabrication, easier to scale up, and fast gate speed, superconducting qubits usually have much shorter decoherence time than trapped ions, NMR etc. due to the relatively strong interactions between qubits and environment. Recent experiments show that low frequency flux noise is the dominant mechanism of decoherence in superconducting flux qubits. However, despite extensive effort the origin of flux noise is still not well understood. The goal of this work is to identify the source and

characterize the property of flux noise in rf SQUID flux qubit through various spectroscopy and time-resolved measurements. Our result show that one can determine all circuit parameters needed for reconstructing qubit Hamiltonian with high accuracy via measurement of macroscopic resonant tunneling (MRT) and photon assisted tunneling (PAT) and that the amount of flux noise in rf SQUID qubits scales linearly with self inductance of the qubits. In addition, we have investigated the dynamics of a three-level flux qubit in incoherent regime. The result demonstrates that treating a multi-level physical qubit, such as the superconducting flux qubit, as an ideal two-level quantum system may be inadequate under certain circumstances.

Acknowledgements

I would like to express my deepest gratitude to my dissertation advisor, Dr. Siyuan Han, for his unlimited support and guidance throughout my entire graduate studies. I would also like to thank our collaborators, Dr. Vijay Patel and Dr. Wei Chen in Dr. James Lukens' laboratory in the State University of New York at Stony Brook, for their great efforts in qubit sample fabrication. I would like to express my thanks to Dr. Yang Yu from Nanjing University for many useful discussions.

My special thanks go to all members of the quantum electronic Laboratory, Dr. Shaoxiong Li, Bo Mao and Matt Matheny for their continuous scientific support and assistance. In particular, I am grateful to Dr. Zhongyuan Zhou for many useful discussions about various qubit models. The work would not be done without their efforts.

I would like to express my appreciation to my dissertation committee members, Dr. Judy Wu, Dr. Philip S. Baringer, Dr. Shih-I Chu and Dr. Hui Zhao for spending time on reading my dissertation and giving me many good suggestions.

I would like to acknowledge with many thanks the help of the supporting team in KU physics: Doug Fay, Allen Hase, Zach Kessler, John Ledford, Jeff Worth, Nicky Kolatch and Teri Leahy for their assistance to my projects. They are all nice people and I enjoyed working with them.

My special gratitude goes to my wife Shinying, my parents and my sisters for their love, understanding and support. I would not have done it without their support and encouragement. Finally, I would like to dedicate this dissertation to my late father Changneng.

This work was partially supported by NSF and AFOSR.

Table of Contents

List of Symbols

d : Phase difference across a Josephson junction

y : Macroscopic wavefunction

r : Density of states

I_c : Critical current of a Josephson junction

I : Bias current of Josephson junction

I_s : Switching current

e : Electron charge, 1.6×10^{-19} C

V : Voltage across the junction

Φ : Total flux enclosed in an rf SQUID

Φ_x : Magnetic flux applied to an rf SQUID

Φ_0 : Magnetic flux quantum, 2.07×10^{-15} Wb

L : Self inductance of an rf SQUID

l : Self inductance of a compound Josephson junction

g : $g = L/l$

h : Plank constant, 6.63×10^{-34} J·s

$\hbar$: $h/2p$, 1.055×10^{-34} J·s

U : Potential energy

R : Shunting resistance of a Josephson junction

C_0: Shunting capacitance of a Josephson junction

b_{L0}: Measurement of the junction's critical current in an rf SQUID

j: Total magnetic flux enclosed in an rf SQUID normalized to $\Phi_0/2p$

j_x: Magnetic flux applied to an rf SQUID normalized to $\Phi_0/2p$

ΔU: Barrier height of a double-well potential

e: Energy bias of a double-well potential

U_{CN}: Matrix representation of the CNOT gate

$|y\rangle$: Eigenstate of a qubit

H: Hamiltonian

p_i: Momentum operator conjugates to Φ_i $(i = x, y)$

Φ_{cjj}: Magnetic flux enclosed in a compound Josephson junction

Φ_{xcjj}: Magnetic flux applied to a compound Josephson junction

j_{cjj}: Magnetic flux enclosed in a compound Josephson junction normalized to $\Phi_0/2p$

j_{xcjj}: Magnetic flux applied to a compound Josephson junction normalized to $\Phi_0/2p$

E_J: Josephson coupling energy

$E_{J\pm}$: Sum and difference of two junctions' Josephson coupling energy

s_i: Pauli matrices, $i = x, y, z$

Δ: Tunnel splitting energy

k_B: Boltzmann constant, 1.38×10^{-23} J/K

T: Temperature

dE_n: Width of n_{th} energy level

Q: Quality factor

Z_0: Qubit characterization impedance

T_{cr}: Classical to quantum crossover temperature

w_0: Plasma frequency

Φ_m: Magnetic flux applied to dc SQUID magnetometer

M_m: Mutual inductance between dc SQUID magnetometer and Φ_m coil

M_{qs}: Mutual inductance between dc SQUID magnetometer and qubit

ΔI_s: The difference of dc SQUID magnetometer switching currents for two qubit states $|0\rangle$ and $|1\rangle$

I_{cir}^q: The circulating current in the qubit

I_{rf_bias}: Pulsed bias current

w_{LC}: SQUID's LC resonance frequency, $w_{LC} \equiv 1/\sqrt{LC}$

$a^+(a)$: Creation (annihilation) operator

R_Q: Resistance quantum, $R_Q \equiv h/4e^2 \simeq 6.45$ kΩ

J: $J \equiv \sqrt{mw_{LC}/\hbar}$

Φ_i^0: Magnetic fluxes $(i = m, x, cjj)$ trapped at zero current bias

c^2: Chi square of a linear fitting of the $\Phi(\Phi_x)$ near $\Phi_x = \pm 0.5\,\Phi_0$

P_s: Survival probability

Γ: Tunneling rate

t_{dwell}: Dwell time

V_0: Voltage bias to initialize the qubit state

V_1: Voltage bias of the flux bias applied to the qubit

$\Delta\Phi_x$: Separation of two adjacent resonant tunneling peaks

$W_{i\to j}^{ph}$: Transition probability from state $|i\rangle$ to state $|j\rangle$

w_{rf}: Angular frequency

$V_{i\to j}$: Tunneling matrix element

J_c: Critical current density

g_1: Energy relaxation rate

g_2: Dephasing rate

T_1: Energy relaxation time

t_{pulse}: Microwave pulse duration

t_{delay}: Delay time of the pulse current bias followed by the falling edge of microwave pulse

g_{ij}: Relaxation rate from i_{th} energy level to j_{th} energy level

R_{eff}: Effective damping resistance

X_{ij}: Reduced tunneling matrix element

r_i: Occupation probability of energy level $|i\rangle$

P_{rf}: Microwave power

a: Microwave to qubit coupling strength

n: Defect density

$M(x,y)$: Mutual inductance between an electron's magnetic moment at (x,y) and a SQUID loop

m_B: Bohr magneton, 9.27×10^{-24} J/T

S_Φ: Spectral density of the flux noise

$\left\langle (d\Phi_{st})^2 \right\rangle$: Total mean square normalized flux noise

Ω_R: Rabi frequency

T_2^*: Decoherence time

f: Frequency

List of Figures

List of Tables

Chapter 1. Introduction

For over two decades, fascinating progress have been achieved since Leggett and his coworkers proposed that a superconducting loop containing a Josephson tunnel junction could exhibit a superposition of two macroscopically distinct quantum states representing clockwise and anti-clockwise rotating supercurrents [1-3]. A number of quantum phenomena, such as macroscopic quantum tunneling [4-8], energy level quantization [9-11], quantum incoherent relaxation [12], macroscopic resonant tunneling (MRT) and photon-assisted tunneling [10], photon induced transitions, and population inversion between macroscopic quantum states [13-15] have been demonstrated. A few years ago, superposition of two macroscopic quantum states [16, 17] and time domain coherent oscillation between two quantum states in various Josephson junction based superconducting circuits were also demonstrated [18-22]. Since superconducting quantum circuits, especially the flux qubit based on SQUID (Superconducting QUantum Interference Device) offer flexibility in design, scalability in fabrication, ease of initialization, state control, single qubit addressability, and single-shot readout they have become one of the most competitive candidates for implementing quantum computation which if realized can solve hard computational problems that no classical computer can tackle. However, comparing to other candidates of qubit, such as nuclear spins and trapped ions which has long coherence time but very difficult to scale up, superconducting qubits suffer

from decoherence due to their relatively strong interaction with environment. At the present time the biggest obstacle of using superconducting flux qubits for quantum information processing is to significantly increase their coherence time. For this purpose we must identify the sources and understand the mechanisms of decoherence in superconducting qubits.

The purpose of this work is to identify the source and characterize the property of flux noise in rf SQUID flux qubits. In this work we performed energy relaxation time (T_1) measurement in time domain and extracted low frequency flux noise from MRT and microwave spectroscopy measurements. The results show that low frequency flux noise is the dominant mechanism of decoherence in superconducting flux qubits and has a linear dependence on inductance of the flux qubits.

1.1 Superconductivity

Ever since the discovery of Superconductivity in 1911 [23], people have put lots of effort into trying to understand the physics behind it, both experimentally and theoretically [24-30]. Among them, are the phenomenological interpretation of superconductivity by Landau and Ginzburg in 1950, and the microscopic picture of superconductivity introduced by Bardeen, Cooper, and Schrieffer in 1957. The Ginzburg-Landau theory had great success in explaining the macroscopic properties

of superconductors and later becomes the foundation of understanding Type I and Type II superconductors predicted by Abrikosov. The BCS theory shows that superconductivity in conventional superconductors is due to electron pairs mediated by electron-phonon interaction. The two electrons have equal and opposite spin and momentum and the electron-electron interaction is through the exchange of phonon energy. When the energy difference between the two electrons is less than the phonon energy, the interaction is attractive. The attractive interaction dominates over the repulsive screened Coulomb interaction and is responsible to bind pairs of electrons into a bound state with binding energy

$$E' = 2E_F - E > 0 \qquad (1.1),$$

where, E_F is the Fermi energy of the Fermi sea of electrons and E is the eigenenergy of the electron pairs, or Cooper pairs. At low temperature Cooper pairs, which are bosons, condense into a single ground state. The superconducting current is a superfluid of Cooper pairs.

1.2 The Josephson Effect

A Josephson tunnel junction consists of a thin insulating layer (tunnel barrier) sandwiched between two superconductors [31, 32]. Cooper pairs that tunnel through a thin insulating barrier form a supercurrent. The dc Josephson effect describes the supercurrent between two superconducting electrodes separated by a thin insulator

barrier as a function of the phase difference between the two electrodes $d = q_2 - q_1$, where q_i $(i = 1, 2)$ are the phases of the two superconductors, whose states are described by the macroscopic wave functions $y_i = r_i^{1/2} \exp(jq_i)$. Supercurrent flowing through the junction is given by:

$$I = I_c \sin d \tag{1.2},$$

where critical current I_c is defined as the maximum supercurrent that the junction can support The time evolution of the phase difference is related to the voltage across the junction V through the so-called Josephson voltage-frequency relation or ac Josephson effect

$$\frac{dd}{dt} = \frac{2eV}{\hbar} \tag{1.3},$$

where $2eV$ corresponds to the energy change of a Cooper pair transferred across the junction.

1.3 RF SQUID

The rf SQUID [32] consists of a superconducting loop of inductance L interrupted by a Josephson junction with critical current I_c. An external flux Φ_x applied to the superconducting loop will induce a persistent current $I_s = I_c \sin(2p\Phi/\Phi_0)$. The macroscopic quantum variable in this system is the total magnetic flux $\Phi = \Phi_x + LI_s$ through the superconducting loop, where $\Phi_0 = h/2e$ is the

flux quantum. Using the resistively shunted junction (RSJ) model [33], the dynamics of an rf SQUID can be described as a particle (with mass C_0) moving in a 1D potential $U(\Phi)$ with damping coefficient R^{-1}. The classical equation of motion (EOM) of a rf SQUID can be written as

$$C_0\ddot{\Phi}+\frac{\dot{\Phi}}{R}=-\frac{\partial U(\Phi,\,\Phi_x)}{\partial\Phi} \tag{1.4}$$

where, C and R are the shunting capacitance and resistance of the Josephson junction respectively. The SQUID potential is given by

$$U(j,\,j_x)=U_0\left[\frac{1}{2}(j-j_x)^2-b_{L0}\cos j\right] \tag{1.5}$$

where, $U_0=(\Phi_0/2p)^2/L$, $b_{L0}=2p\,LI_c/\Phi_0$ is a measure of the junction's critical current I_c in terms of the current required to create one flux quantum in the loop, and $j=(\Phi/\Phi_0)2p$ and $j_x=(\Phi_x/\Phi_0)2p$ are the normalized total and external magnetic fluxes in unit of $\Phi_0/2p$. When b_{L0} is greater than unity, the potential can have metastable states. The shape of the potential is determined by the parameters L, C_0, R, b_L and Φ_x. At $j_x/2p=(n+1/2)$, U is a bounded symmetric double-well potential. By tuning the external flux away from $(n+1/2)\Phi_0$, the double-well potential is tilted. Such a tilted double-well potential is shown in Figure 1.1 with $\Phi_x=0.475\,\Phi_0$ and $b_{L0}=2$. The left and right wells correspond to the SQUID being

in different fluxoid states $|0\rangle$ and $|1\rangle$, with supercurrent flowing in opposite directions.

1.4 Quantum Computation

1.4.1 Quantum Bit (Qubit)

An ideal qubit is a two-state quantum system, with two basis states $|0\rangle$ and $|1\rangle$. Unlike a classical bit, which can be in only one of the two available states at a time, a qubit can be in a linear superposition of the two basis states

$$|y\rangle = a|0\rangle + b|1\rangle \qquad (1.6),$$

where, a and b are called probability amplitude and in general are complex numbers. Hence, $|a|^2$ ($|b|^2$) is the probability of finding the system in the state $|0\rangle$ ($|1\rangle$) and $|a|^2 + |b^2| = 1$.

1.4.2 Quantum logic gate

In gate model quantum computing, quantum information is processed by a series of quantum logic gates. A quantum logic gate is a unitary transformation on a set of qubits. Generally, an arbitrary quantum computation on any number of qubits can be generated by a finite set of gates, including single qubit gates and any type of

2-qubit gate [34, 35]. The most common single qubit gate is the NOT gate (denoted as X). The matrix representation of the NOT gate is given by

$$X \equiv \begin{bmatrix} 0 & 1 \\ 1 & 0 \end{bmatrix} \tag{1.7}$$

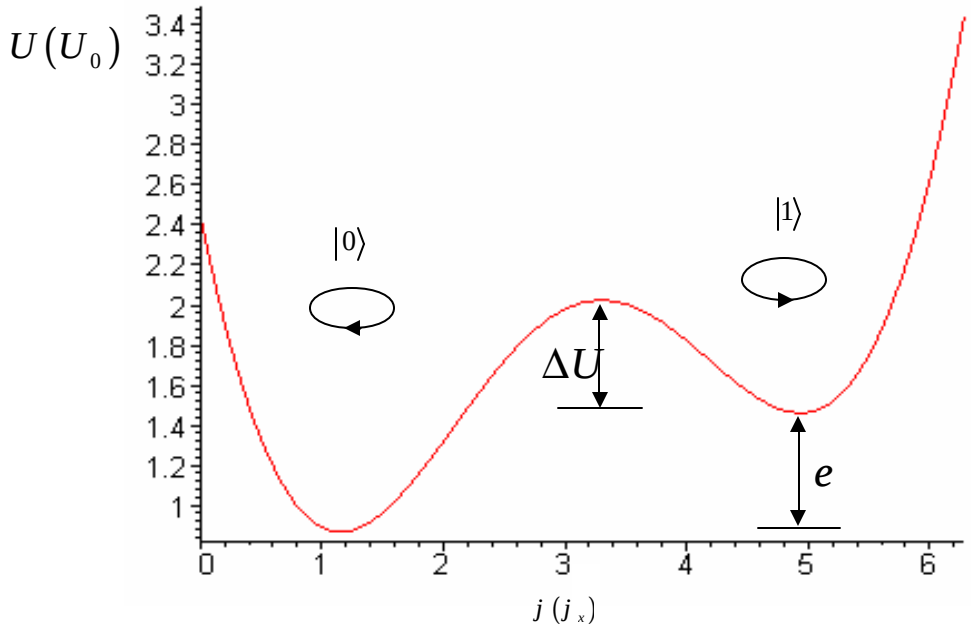

FIG. 1.1. The double well potential of an rf SQUID at $\Phi_x = 0.475\,\Phi_0$ and $b_{L0} = 2$. $|0\rangle$ and $|1\rangle$ fluxoid states represent supercurrent flowing in opposite directions in the superconducting loop of the SQUID.

The prototypical 2-qubit quantum logic gate is the controlled-NOT gate or CNOT gate. A CNOT gate is a quantum gate with two qubits, known as the *control qubit* (control bit) and *target qubit* (target bit), respectively. The action of the CNOT can be expressed by $|c\rangle\ |t\rangle\ \rightarrow\ |c\rangle\ |t \oplus c\rangle$, where $\oplus$ denotes addition modulo two. The state of the target bit after the operation depends on the state of the control bit, if the control bit is in the $|0\rangle$ state, the target bit will not change its state. However, when the control bit is in the $|1\rangle$ state, after the gate operation, the state of the target bit will change from $|0\rangle$ to $|1\rangle$ or $|1\rangle$ to $|0\rangle$. The truth table of the CNOT gate is given by

$$\begin{array}{cc} \text{C} & \text{T} \\ |0\rangle & |0\rangle \\ |0\rangle & |1\rangle \\ |1\rangle & |0\rangle \\ |1\rangle & |1\rangle \end{array} \rightarrow \begin{array}{cc} \text{C} & \text{T} \\ |0\rangle & |0\rangle \\ |0\rangle & |1\rangle \\ |1\rangle & |1\rangle \\ |1\rangle & |0\rangle \end{array} \tag{1.8}$$

where C (T) denotes the control (target) bit. The matrix representation of the controlled-NOT gate, U_{CN}, is given by

$$U_{CN} = \begin{bmatrix} 1 & 0 & 0 & 0 \\ 0 & 1 & 0 & 0 \\ 0 & 0 & 0 & 1 \\ 0 & 0 & 1 & 0 \end{bmatrix} \tag{1.9}$$

The qubit state can be expressed as a vector $|y\rangle$ pointing to the surface of the Block sphere (Figure 1.2) in terms of angles f_1 and f_2 as described by [36]:

$$|y\rangle = \cos\frac{f_2}{2}|0\rangle + e^{if_1}\sin\frac{f_2}{2}|1\rangle \qquad (1.10),$$

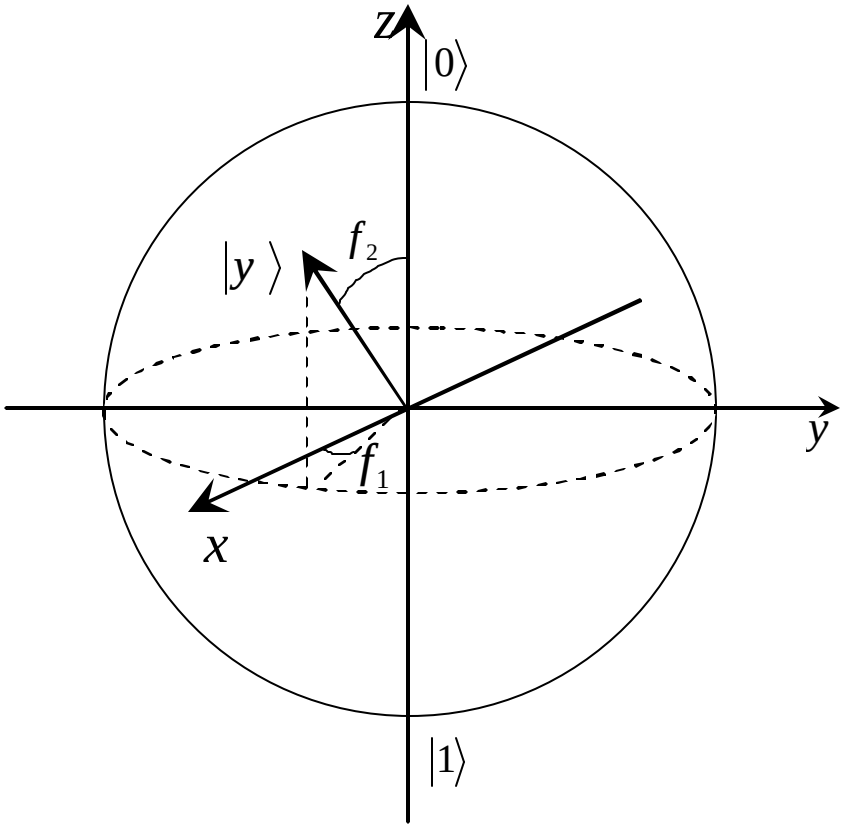

FIG. 1.2. Bloch sphere

1.5 Tunable Δ rf SQUID as flux qubit

In our experiment, the single junction was replaced by a compound Josephson junction [10, 12-14, 16, 37]. The compound junction consists of two Josephson junctions in parallel enclosed in a small superconducting loop of inductance l. The Hamiltonian of an isolated rf SQUID with zero dissipation is given by

$$H = \frac{p_\Phi^2}{2C} + U(\Phi) \tag{1.11}$$

where $C = 2C_0$ (assumed two Josephson junctions are equal). The potential energy of an rf SQUID with a compound junction, which consists of two junctions in a small loop, replacing the single junction is given by

$$U = \frac{(\Phi - \Phi_x)^2}{2L} + \frac{(\Phi_{cjj} - \Phi_{xcjj})^2}{2l} - E_{J+}\cos\left(p\frac{\Phi_{cjj}}{\Phi_0}\right)\cos\left(2p\frac{\Phi}{\Phi_0}\right) + E_{J-}\sin\left(p\frac{\Phi_{cjj}}{\Phi_0}\right)\sin\left(2p\frac{\Phi}{\Phi_0}\right) \tag{1.12}$$

here, Φ and Φ_{cjj} are the total magnetic fluxes in the rf SQUID and the small loop formed by the compound junction, respectively. Φ_x and Φ_{xcjj} are the magnetic fluxes applied to the rf SQUID loop and the small compound junction loop. The kinetic energy terms are

$$\frac{p_x^2}{2m_x} = -\frac{\hbar^2}{2(2C_0)}\frac{\partial^2}{\partial j_x^2} \tag{1.13a}$$

$$\frac{p_{cjj}^2}{2m_{cjj}} = -\frac{\hbar^2}{2(C_0/2)}\frac{\partial^2}{\partial j_{cjj}^2} \tag{1.13b}$$

where $E_{J\pm} = E_{J1} \pm E_{J2}$ are the sum and difference of the two junctions' Josephson coupling energy as defined by $E_J = \hbar I_c / 2e$. This potential can also be written as

$$U = U_0 \left[\frac{1}{2}(j - j_x)^2 + \frac{g}{2}\left(j_{cjj} - j_{xcjj}\right)^2 - b_+ \cos\left(\frac{j_{cjj}}{2}\right)\cos j + b_- \sin\left(\frac{j_{cjj}}{2}\right)\sin j \right] \tag{1.14},$$

where, $U_0 = \dfrac{\Phi_0^2}{4p^2 L}$, $b_\pm = b_1 \pm b_2 = 2pL\left(I_{c1} \pm I_{c2}\right)/\Phi_0$, $g = L/l$. j, j_x, j_{cjj} and j_{xcjj} are the normalized form of Φ, Φ_x, Φ_{cjj} and Φ_{xcjj} in units of $\Phi_0/2p$. The dynamic variable j describes the in-phase motion of the compound junction which results in a circulating current in the large loop while j_{cjj} describes the out of phase motion that results in a circulating current in the small loop. Note that $m_x = 4m_{cjj}$ as the circulation current in the big loop sees the two junctions in parallel while that in the small loop sees them in series. The model can be readily generalized to junctions having not only different I_c, but also unequal capacitances and asymmetric small loop inductance. However, as variations in C_0 and l are much less than that in I_c for real devices, their effects are usually negligible. Equation (1.14) can be further reduced to a simpler form by eliminating the term containing b_- when the two junctions are identical. The Hamiltonian of the system is determined by a total of five independent device parameters which can be chosen as L, C_0, g, and $b_\pm$. In the limit of $L/l >> 1$ one has $j_{cjj} \approx j_{xcjj}$ and the potential can be approximated very well by the

1D potential of Equation (1.5) with $b_L = b_+ \cos j_{xcjj}$. The tilt (e) and tunnel splitting (Δ) of the double well potential can be tuned *in situ* by adjusting Φ_x and Φ_{xcjj}, respectively.

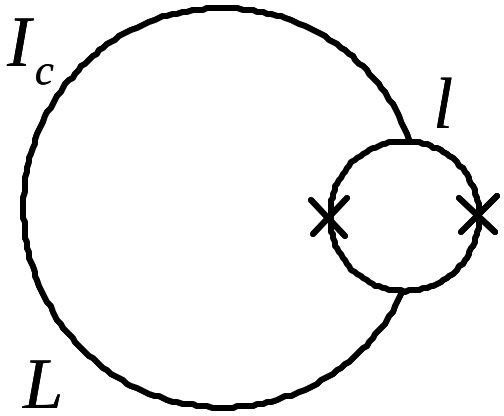

FIG. 1.3. Schematic drawing of a tunable Δ rf SQUID

1.5.1 The Two-level qubit

In general, a dissipative quantum two-level system (TLS) can be described by the "spin-boson" model developed by Leggett *et al.* [38]. The Hamiltonian of a TLS can be written in the spin-1/2 notation as:

$$H = -\frac{1}{2}(e\hat{s}_z + \Delta\hat{s}_x) \tag{1.15}$$

and $\hat{s}_i$ $(i = x, y, z)$ are the Pauli matrices. In the rf SQUID, at low temperatures, only the lowest energy states in the two wells contribute, while all excited states can be ignored. In this case, the rf SQUID is reduced to a two-state quantum system which can be described by Equation (1.15). The diagonal term e in the Hamiltonian is proportional to the applied flux Φ_x which sets the tilt of the double-well potential. The off-diagonal term Δ is the tunneling amplitude between the wells which depends on the barrier height exponentially. $E_{0,1} = \pm\frac{1}{2}\sqrt{e^2 + \Delta^2}$ are the eigenenergies of the two energy eigenstates $|0\rangle$ and $|1\rangle$.

1.5.2 The Three-level flux qubit

However, a physical qubit, for instance an rf SQUID flux qubit, has more than two levels. Dipole coupling between qubit's two-computational states to its noncomputational states could lead to significant problems, such as intrinsic gate error and leakage to the noncomputational states during qubit manipulations [39], and

multiphoton transitions in the presence of a strong field [40-45]. In order to address these issues, a Λ-type three-level SQUID flux qubit has been proposed recently [46-48], which has advantages over the traditional two-level qubit. In a three-level qubit an auxiliary level is utilized to greatly increase the value of $\Omega_R T_1$, where Ω_R and T_1 are the frequency of Rabi oscillation and energy relaxation time between the two computational states respectively. It is therefore important to understand dynamics of a three-level flux qubit.

1.5.3 Mechanisms of decoherence

In a real qubit system, coherence between macroscopic quantum states can be destroyed by decoherence such as dephasing and energy relaxation [49, 50]. A recent study shows that dielectric loss from insulating material or inside the tunnel barrier can also lead to short coherence times [51]. In superconducting qubits based on Josephson junctions, several sources of dephasing have been discussed, such as 1/f background charge fluctuation, bias flux fluctuation, and critical current fluctuation [52-55]. Energy relaxation which results in spontaneous decay of the qubit states is due to and proportional to dissipation. For a sufficiently isolated superconducting qubit dissipation broadens the energy levels so that the lifetime of the excited states becomes finite. Theory predicted that at low temperatures, where the energy level spacing is much larger than $k_B T$, the width of the n-th excited state is given by

$dE_n \simeq E_n/Q$ [56, 57], where Q is the quality factor of the classical small-amplitude oscillations in the potential well. It should be noted that as the level of damping is increased quantum coherence will be destroyed but other distinct quantum effects, such as energy level quantization and resonant tunneling between quantized energy levels, can be preserved.

Chapter 2. Experimental Setup

The qubit is an rf SQUID that consists of a large superconducting loop interrupted by a compound junction (as shown in Figure 2.1). The flux signal induced by the changes of qubit supercurrent as the qubit changes the state (from $|0\rangle$ to $|0\rangle$ or visa versa) will be captured by an inductively coupled superconducting quantum interference device (dc SQUID) magnetometer. The qubit circuits, which include the qubit, dc SQUID magnetometer, flux control lines, and coplanar waveguide (CPW) for state manipulation with microwave, were fabricated using a self-aligned lift-off (SAL) process [58, 59] by Prof. Lukens' group at the State University of New York at Stony Brook. Considerations have been given to minimizing external noise and increasing the signal-to-noise ratio of the qubit signal detected by the magnetometer. For instance, in order to obtain the appropriate coupling strength between the magnetometer and the qubit, their loops partially overlap each other, which results in a mutual inductance of 23.4 pH. Another example is the adoption of a 2^{nd} order gradiometer configuration in the qubit design to null out the effect of large scale flux noise.

2.1 Sample Design

The qubit sample is mounted inside a niobium (Nb) sample cell thermally anchored to the mixing chamber of an Oxford Kelvinox 400 dilution fridge. The flux bias Φ_x and the microwave are coupled to the qubit via thin film gradiometer coils on the same chip.

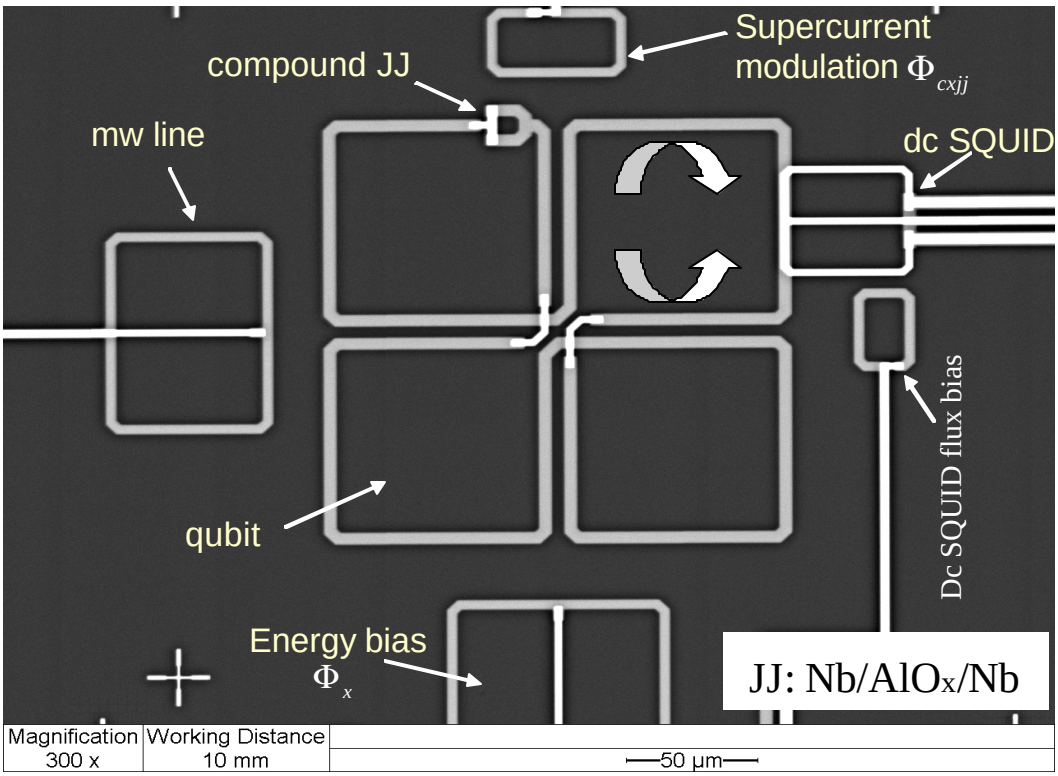

FIG. 2.1. SEM image of an rf SQUID qubit with 2nd order gradiometer configuration, its flux control coils, and dc SQUID magnetometer.

2.1.1 Qubit

The dimension of the 2^{nd} order gradiometer is $180\times180\ \mu m^2$ with $5\ \mu m$ linewidth. The self inductance of the loop is $L=1077\ pH$, which is calculated using the MIT Fasthenry program. To adjust the Josephson coupling energy *in situ* the qubit superconducting loop is interrupted by a low inductance ($l=18\ pH$) compound junction (dc SQUID). Figure 2.1 shows the SEM image of an rf SQUID qubit circuit. Because $L/l>>1$, a one dimensional (1D) potential is therefore an excellent approximation to the exact 2D qubit potential [60]. The external flux bias Φ_x is applied through a gradiometer coil, which is placed $24\ \mu m$ away from the qubit loop with self inductance of $135\ pH$. The mutual inductance between the qubit and the Φ_x line is $1.17\ pH$, which is determined from the periodicity of the transition between the two qubit states near $\Phi_x=\Phi_0/2$ as shown in Figure 2.2.

The Josephson coupling energy of the compound junction is controlled by a flux Φ_{cjj} generated by an on-chip single turn coil. The distance between the compound junction and Φ_{cjj} coil is $12\ \mu m$ and the mutual inductance is about 0.4 pH.

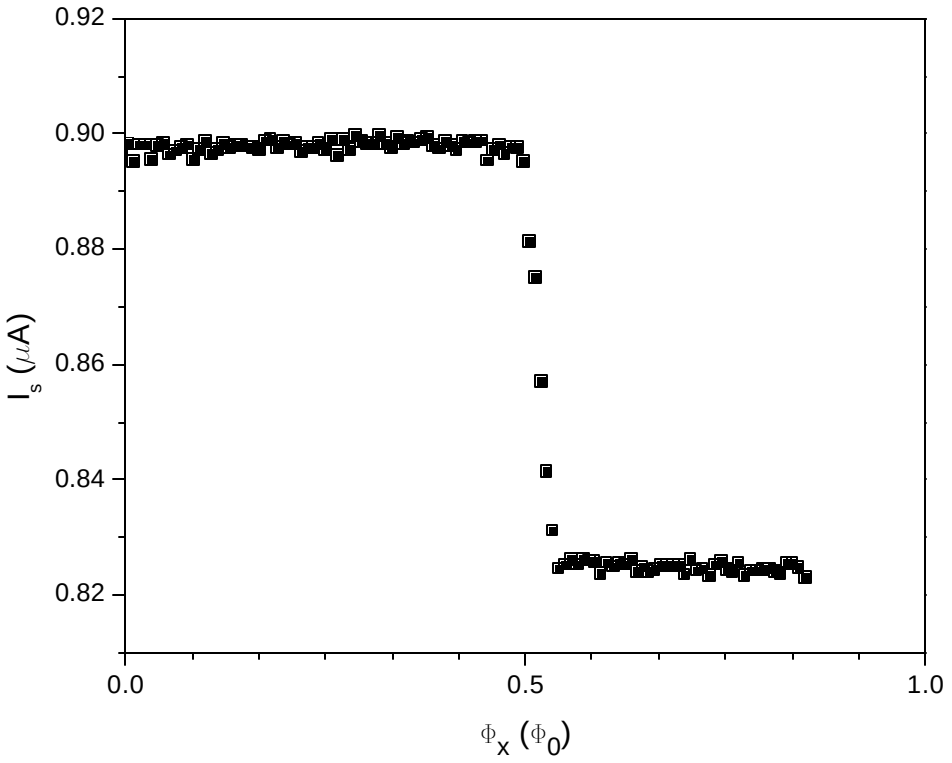

FIG. 2.2. Transition steps between the qubit's two flux states distinguished by the magnetometer.

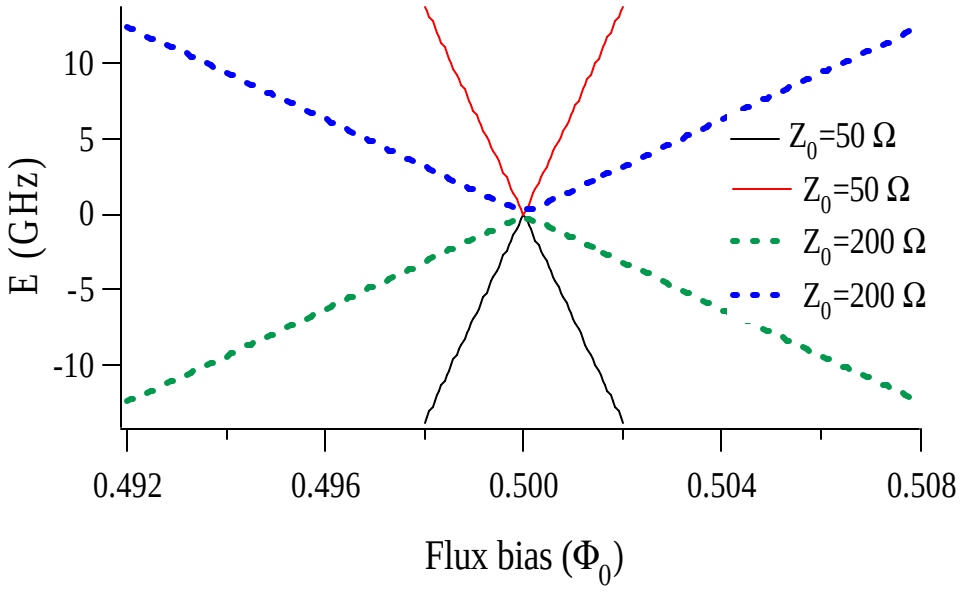

FIG. 2.3. The first two energy levels as a function of flux bias near $\Phi_0/2$ for two different values of qubit characteristic impedance.

The large 2nd order gradiometer configuration served the following purposes:

1. To reduce the effect of low frequency flux noise on dephasing (Figure 2.3). Increasing the qubit characteristic impedance $Z_0 = \sqrt{L/C}$ makes the qubit less sensitive to the low frequency flux noise as the rate of dephasing depends linearly on the slope of the qubit energy level which is inversely proportional to the qubit characteristic impedance: $\partial E / \partial \Phi_x \propto Z_0^{-1}$.
2. To make the qubit insensitive to ambient magnetic field fluctuations.

2.1.2 The Magnetometer

An underdamped dc SQUID magnetometer with a hysteretic current-voltage characteristic inductively coupled to the qubit is used to read out the qubit state. The magnetometer consists of two Josephson junctions in parallel, each having a capacitance $C = 90$ fF in a superconducting loop. The self inductance of the loop, $L_s = 120$ pH. The total critical current, $I_c = 2.18$ μA, (assuming two identical junctions) are determined by comparing the width of the switching current distribution measured at a temperature well below the quantum-classical crossover temperature, $T_{cr} = \hbar w_0 / 2p k_B$, to the MQT theory [61]. The dynamics of the dc SQUID can be described as a particle of mass $2C$, moving in a 2D potential [32, 62, 63]. The current through the dc SQUID has two components. A circulation current, I_{cir}^s, corresponds to the flux induced in the SQUID and a common mode current

equals to the bias current, I. An external flux coil Φ_m placed $5\,\mu m$ away from the dc SQUID was used to apply a magnetic flux Φ_m to it. When a constant bias current I is applied to the dc SQUID, its switching current oscillates as a function of Φ_m as shown in Figure 2.4.

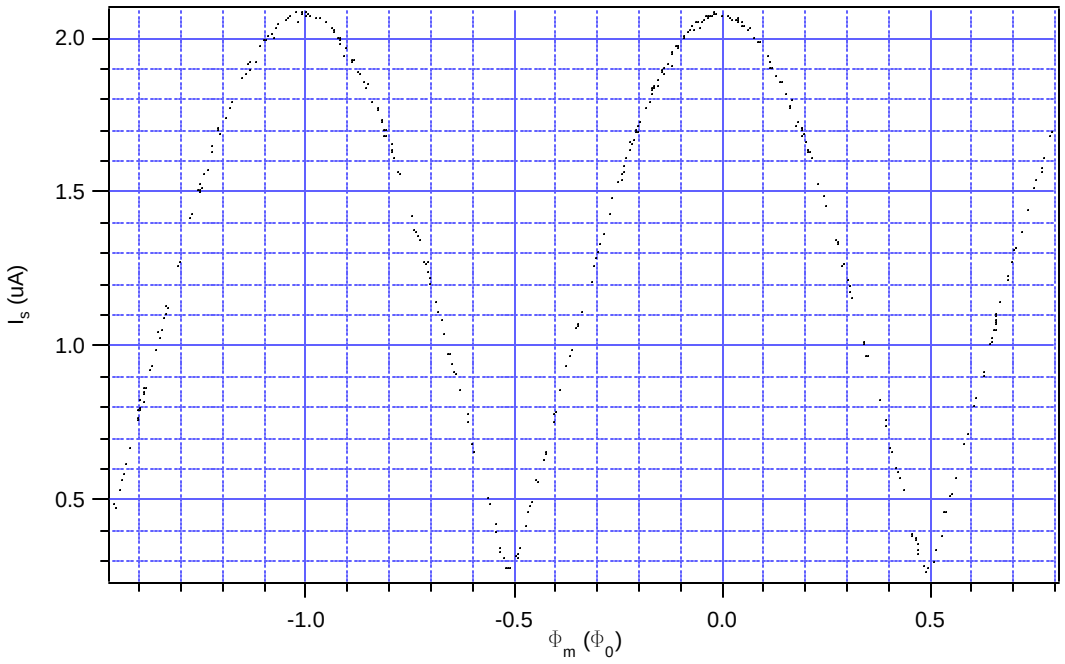

FIG. 2.4. Measured dc SQUID magnetometer flux-switching current transfer function of sample (VJKQC4-3-40) at T=30 mK. The mutual inductance $M_m = 2.14\,pH$ is obtained from the periodicity.

2.1.3 Single Shot Readout

The mutual inductance between the qubit and the dc SQUID is $M_{qs} = 23.4$ pH (within 10% of the value estimated from Fasthenry). This coupling strength is obtained by measuring the difference between the dc SQUID's mean switching current, ΔI_s, when the direction of qubit circulation current is reversed. It is straightforward to show:

$$\Delta I_s \simeq M_{qs}\left[I_{cir}^{q}(1) - I_{cir}^{q}(0)\right]\left(\partial I_s / \partial \Phi_m\right) \qquad (2.1),$$

where, I_{cir}^{q} is the circulating current in the qubit loop and $\partial I_s / \partial \Phi_m$ is the slope of the dc SQUID's current-flux transfer function. For example, in Figure 2.2, the height of the step at $\Phi_0/2$ is $\Delta I_s \simeq 70$ nA, which occurs when the qubit switched from one fluxiod state to the other. Figure 2.5 shows that the qubit state can be determined from a single-shot measurement by ramping the bias current up to 0.94 μA.

2.1.4 On-chip microwave coupling

An on-chip microwave line is placed 20 μm away from the qubit loop with a mutual inductance of 1.38 pH. It is connected to a semi-rigid microwave coaxial cable via an on-chip superconducting coplanar waveguide (CPW) and is wire bonded to an interconnection CPW on a PCB, where the central conductor of the semi-rigid microwave coaxial cable is soldered to the central conductor of the CPW on the PCB

while the ground plane of the CPW is grounded to the Nb sample block. Both of the on-PCB and on-chip CPWs are designed to have a characteristic impendence of $50\,\Omega$.

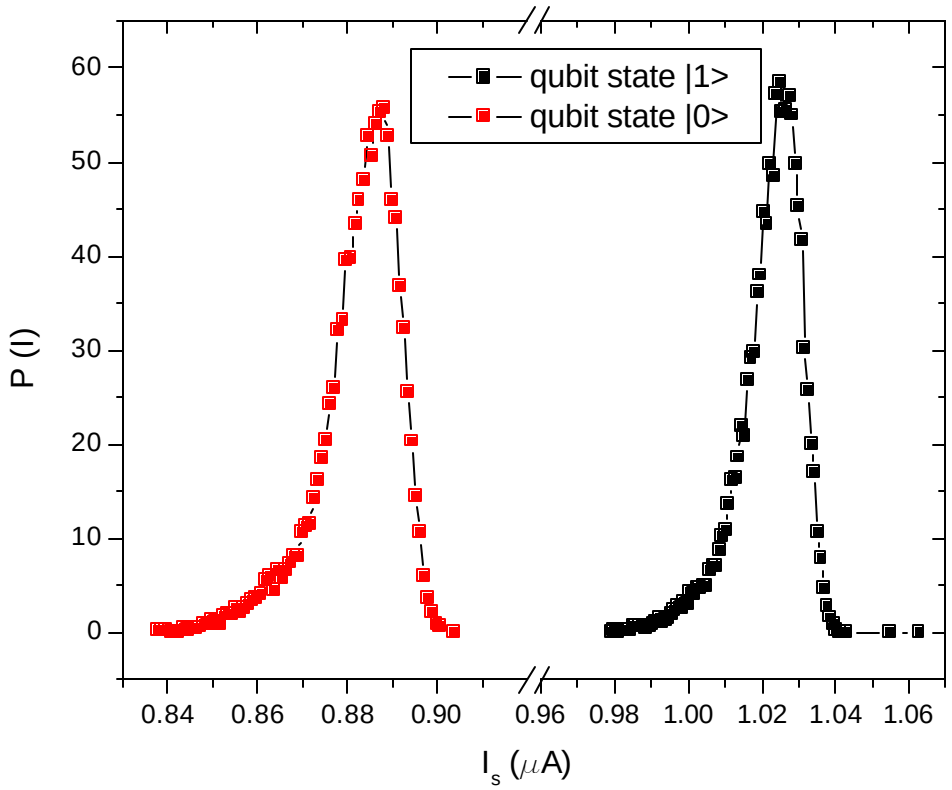

FIG. 2.5. Plot of the histograms of the dc SQUID switching current distribution, where it clearly showed that two fluxoid states $|0\rangle$ and $|1\rangle$ of the qubit can be distinguished by the dc SQUID.

2.2 Experiment Design

2.2.1 Filters

To protect the qubit from extraneous noise from the environment, several filters were used in series inside the dilution fridge [22, 61, 64, 65] (Figure 2.8). A 24-channel discrete-element RC low pass filter is thermally anchored at 1K pot. Each current and voltage channel contains a RC network with a cutoff frequency of ~ 5 kHz. The capacitors have been tested at about 1.5 K, showing no change of their values. $10\,\mathrm{k}\Omega$ metal film resistors were used for the magnetometer dc current bias and voltage signal channels. For Φ_m, Φ_x and Φ_{xcjj} flux bias lines, since a few milliamps of current is needed for the experiment, $1\,\mathrm{k}\Omega$ resistors were used. At higher frequencies, the attenuation decreased dramatically, due to stray capacitance across the resistors and twisted pairs. We found that it is very important to make a very good thermal anchor, otherwise the power dissipated in the resistors could drive the superconducting wires normal all the way down to the sample cell.

To attenuate blackbody radiation from wires at higher temperatures a 12-channel microwave copper powder filter (CPF) [66] has been constructed for the experiment. The CPF consists of 12 NbTi wire spiral coils inside a copper box filled with 325 mesh Cu powder with grain size of $3.25 \sim 4.5\ \mu$m. The CPF is equipped with two Cinch connectors, as displayed in Figure 2.6, and was thermally anchored at the mixing chamber. As each grain appears to be insulated from its neighbors by its surface oxide layer, the large surface area produces a tremendous attenuation. The

measured attenuation of such a filter is greater than 90 dB at 1.4 GHz. Figure 2.7 shows an example of the measured transmission coefficient of a CPF using a 5 feet long, 0.0055" diameter NbTi superconducting magnet wire. The diameter of the spiral coil is ~ 0.1". The main propose of using NbTi wire is to avoid Joule heating from the dc bias current lines as NbTi is superconducting below 10 K.

2.2.2 Sample Cell

The qubit chip is mounted on an Au plated oxygen free copper (OFC) block using GE varnish. The block is assembled inside an Nb sample cell with two 0-80 OFC screws. The sample cell, which is equipped with three SMA connectors, becomes superconducting below 9.2 K and will shield the qubit chip from fluctuations of ambient magnetic field. The Nb sample cell and the 12-channel microwave CPF were mounted to a Au plated OFC platform thermally connected to the bottom of the mixing chamber of the dilution refrigerator (Figure 2.6) whose base temperature is ~ 6 mK. Two more 0-80 OFC screws were used to thermally anchor the OFC block. The temperature can be regulated up to 1.5 K by a heater attached to the mixing chamber using a PID controller. The qubit circuit is connected to a PCB board through Al wiring bonding. The dielectric constant of the PCB board is similar to the Si substrate to reduce impendence mismatch. The leads on the PCB board were then connected to the CPF and the external measurement circuit through a PCB

interconnection bridge. The Al bonding wires also become superconducting when the temperature is below 1.14 K. The measured self inductance of each Al wire is about $1\ \mathrm{nH/mm}$.

The fridge is inside a dewar which is mounted on a vibration-free stage. Two Mu-metal cylinders surround the inner and outer vacuum cans to form magnetic shields. The still radiation shield is Pb plated. A cryoperm cylinder was placed outside the inner vacuum can to further attenuate ambient magnetic fields. All electrical wires from the chip to room-temperature measurement electronics are filtered with electromagnetic interference (EMI) filters at the top of the cryostat at room temperature. A solid copper shielded room equipped with double-shielded cables and shielded metal connectors formed a continuous conducting enclosure that extended from the sample block to the battery-powered part of the setup.

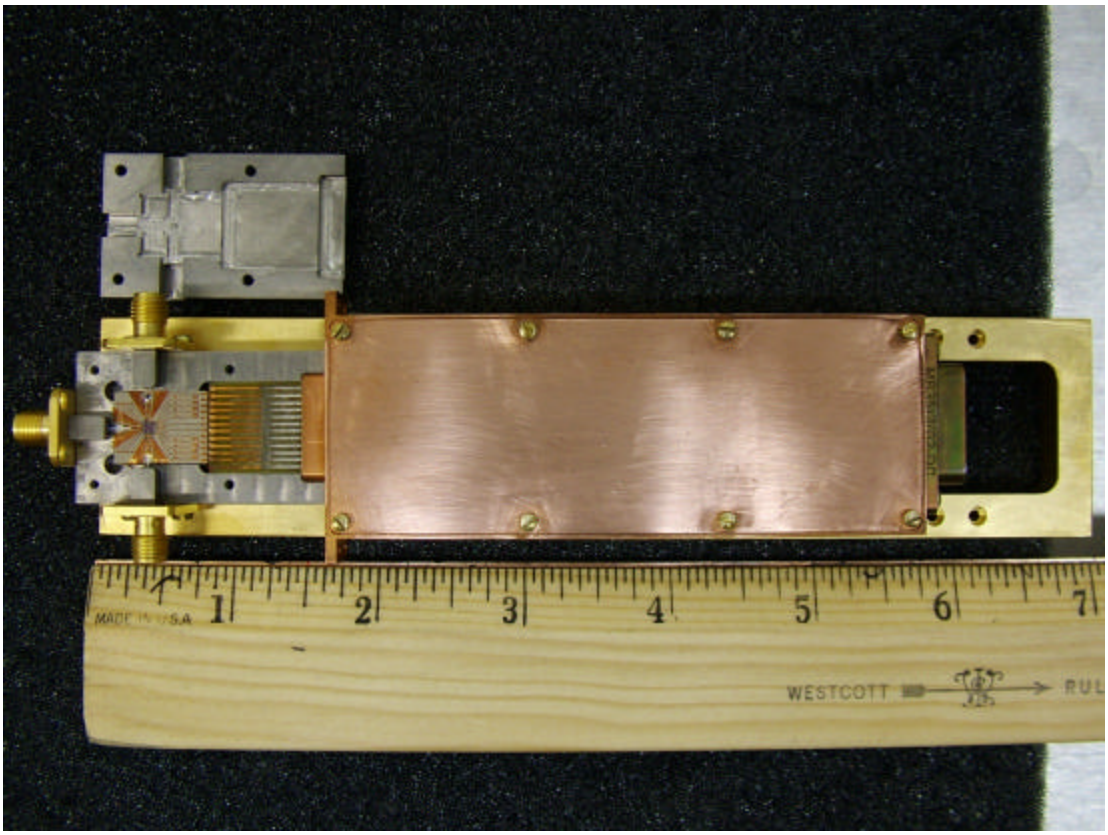

FIG. 2.6. Assembled Nb sample cell (left) with low pass cooper powder filter (right) on the Au plated copper plate.

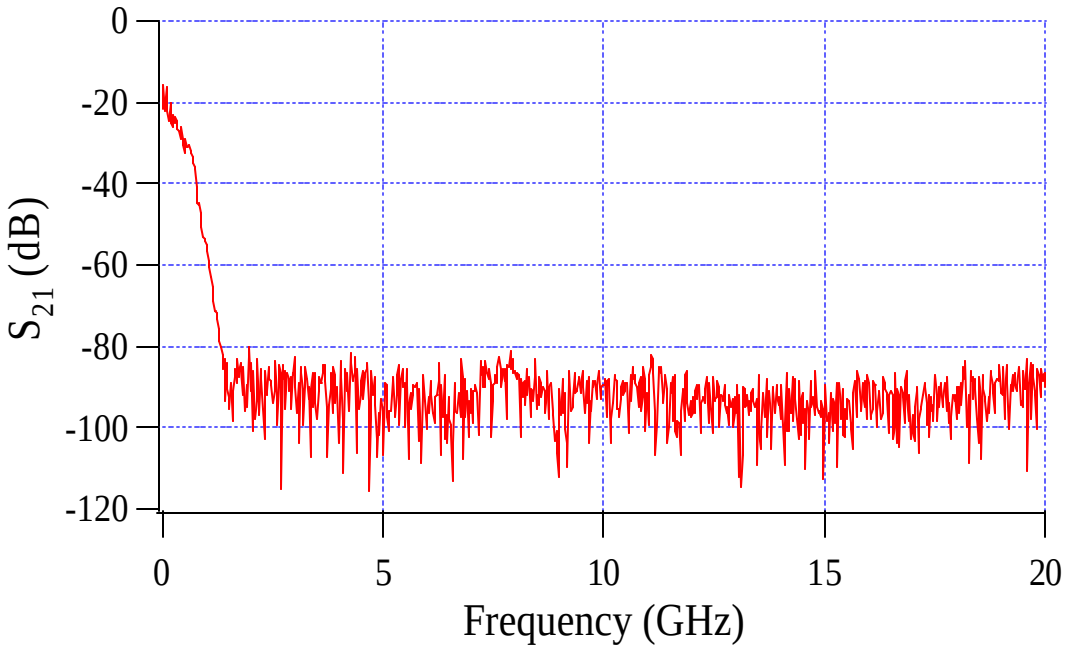

FIG. 2.7. Measured transmission coefficient of the Cu powder filter. The sensitivity of the network analyzer on S_{21} measurement is about -90 dB.

2.3 Measurement Setup

2.3.1 The Electronics

A cryogenic coaxial cable with superconducting NbTi-in-CuNi matrix inner conductor and braided CuNi outer shield [67] with the characteristic impedance $Z = 50\,\Omega$, were installed in the fridge as a pulsed bias current channel, I_{rf_bias}, in addition to the dc current bias line connected to a single ended dc SQUID magnetometer. It was anchored carefully at different temperature stages and was connected to the top of the CPF before entering the Nb sample cell (Figure 2.6).

The pulsed bias current for readout dc SQUID is supplied by a 200 MHz Tektronix arbitrary waveform generator (Tektronix AWG420) with maximum output voltage of 2V. A $50\,\Omega$ semi-rigid coaxial cable goes from the generator to one of the superconducting NbTi pulse lines via a SMA connector at the top of the fridge. A $10\,\mathrm{k}\Omega$ resistor (RR1220P-103-B-T5) is used inside the Nb sample cell to limit the current on the device.

The dc bias current was supplied by the same source, but connected with a $50\,\Omega$ TNC cable through EMI filters before entering the fridge. The current bias level applied to the dc SQUID was calibrated using an HP3458A multi-meter by monitoring the voltage across a $1\,\mathrm{k}\Omega$ resistor at room temperature. When the dc SQUID switched to the finite voltage state, the voltage signal across the dc SQUID was sent to an Agilent 53131A universal counter/timer through a low noise voltage preamplifier (Stanford Research SR560).

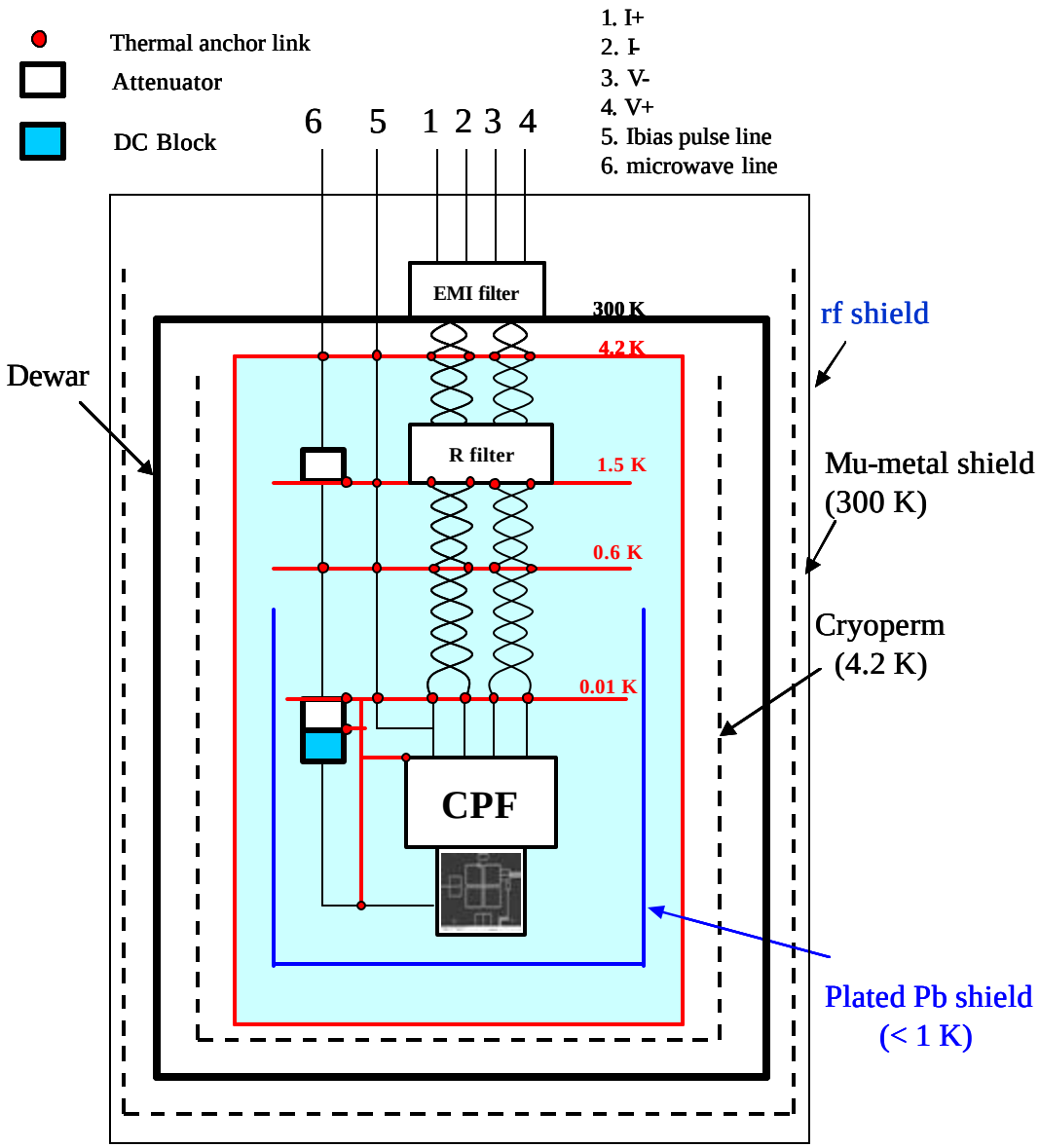

FIG. 2.8. Schematic of the mK qubit experimental set-up.

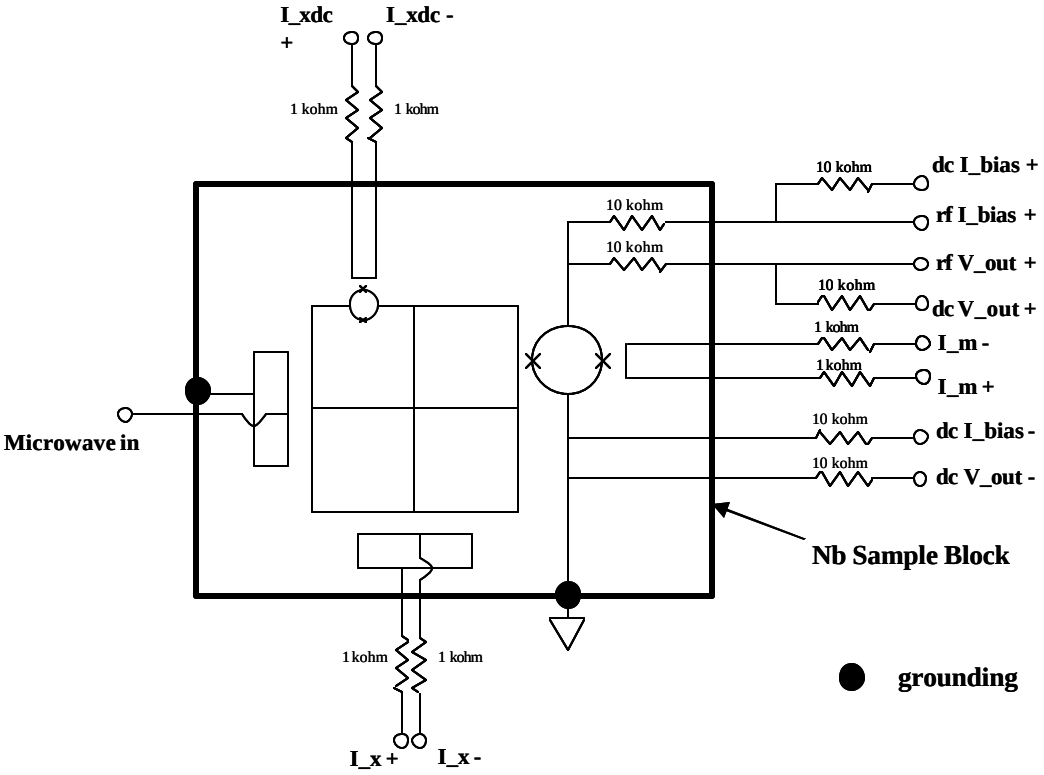

FIG. 2.9. Schematic of qubit circuit inside Nb sample block

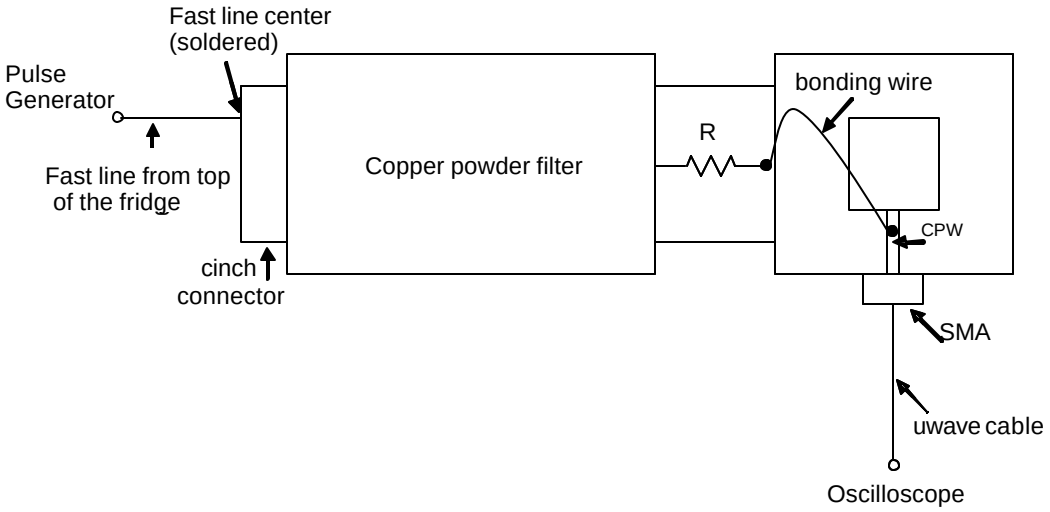

FIG. 2.10. Schematic drawing of the dc SQUID fast bias current channel in the fridge.

The direction of the current circulating in the qubit loop, clockwise or counterclockwise, represents the qubit in the $|0\rangle$ or $|1\rangle$ state. The flux change induced from the change current direction can be detected by the inductively coupled dc SQUID. Therefore, the qubit state can be distinguished by measuring the switching probability of the dc SQUID. To read out the state of the qubit, a 30-ns current pulse was applied to the dc SQUID through the pulsed bias current line (Figure. 2.9). The amplitude of the applied current pulse to the dc SQUID was selected (dashed line in Figure 2.11) by measuring the switching probability as a function of pulse amplitude for each qubit state. Following the short bias current pulse is a few tens of micro-seconds of plateau with the amplitude just above the re-trapping current of the dc SQUID. The purpose of this plateau is to allow the readout electronics at room temperature to have enough time to record the switched event as the bandwidth of the readout electronics is ~ 5 kHz.

The computer and all ac-powered instruments were placed outside the shielded room. Measurements of the dc SQUID voltage noise spectrum showed no peak at 60 Hz and its harmonics. Extensive tests were performed using low critical current junctions to ensure that extraneous noise was negligible down to 10 mK.

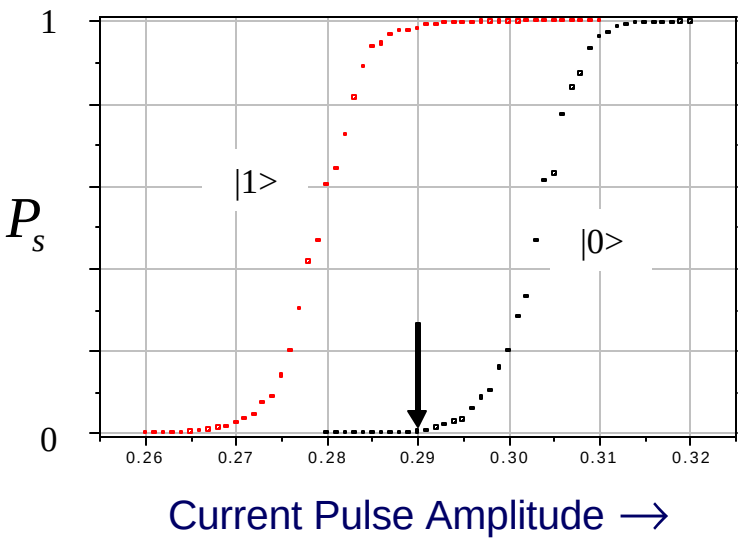

FIG. 2.11. dc SQUID switching probability as a function of the amplitude of the applied current pulse through the current pulse bias line. $|0\rangle$ ($|1\rangle$) correspond to the qubit state with counterclockwise (clockwise) circulation current.

2.3.2 Microwaves

Microwaves were applied to the qubit to induce transitions between qubit energy levels when the microwave frequency matches the level spacing. In order to reduce noise coupled to the qubit, the microwave line was attenuated by two 20 dB attenuators (ATT-0275-20-SMA-02), which were thermally anchored at 1K pot and mixing chamber respectively. All the attenuators and dc block have been tested at < 4.2 K to ensure that they are working properly for cryogenics applications.

To generate nanoseconds microwave pulses, the output of an Agilent E8251 20 GHz synthesizer operated in CW mode was fed to the radio frequency (RF) port of an M/A-COM MY85C mixer. The mixer's IF (intermediate frequency) was connected to the output of an Agilent 81110A pulse/pattern generator with a frequency range of 1 mHz to 330 MHz. The mixer's LO (local oscillator) port then output pulsed microwaves, whose width was defined by the width of the pattern generator TTL pulse. The timing of the pulse is synchronized by the marker, which is a TTL pulse from the AWG. The shortest pulse width obtained with this setup was 1.515 ± 0.25 ns.

Chapter 3. Experimental Procedure and Results

The complete energy level structure of an rf SQUID is determined by the energy eigenvalues and eigenvectors of the rf SQUID Hamiltonian (1.14). Once we have the complete knowledge of the Hamiltonian, we can quantitatively investigate the quantum dynamics of the qubit. An important property of rf SQUID is that all rf SQUIDs with the same "potential shape parameter", b_{L0}, and the same "characteristic impedance", $Z_0 \equiv \sqrt{L/C}$ share a common set of eigenvectors and their eigenenergies are identical when normalized to each SQUID's LC resonance frequency $w_{LC} \equiv 1/\sqrt{LC}$. Reconstructing the SQUID Hamiltonian with parameters b_{L0} and Z_0, along with the energy scale parameter w_{LC}, rather than the original device parameters, is more fundamental to the rf SQUID qubit design, data analysis, and the interpretation of experimental results.

In this chapter, we show first how to obtain the SQUID parameters b_{L0}, Z_0, and w_{LC} from macroscopic resonant tunneling as well as photon assist tunneling. The in-well energy relaxation time is then inferred from measuring the inter-well energy relaxation time. The implementation of three Λ-shaped energy levels of a multilevel rf SQUID qubit will also be presented for the sake of circumventing the problems of two-level SQUID qubits discussed previously.

3.1 Reconstruct the qubit Hamiltonian

When two of the Josephson junctions of the compound junction are identical, the Josephson coupling energy $E_{J+} = E_{J1} + E_{J2}$ and $E_{J-} = 0$. The Hamiltonian (Equation 1.14) can be rewritten in the following form

$$H(x) = \frac{p_x^2}{2m} + \frac{1}{2} m w_{LC}^2 x^2 - E_J \cos\left[2p\left(x + j_x\right)\right] \qquad (3.1),$$

where, $m \equiv C\Phi_0^2$, $x \equiv \left(\Phi - \Phi_x\right)/\Phi_0 = j - j_x$, and $E_J = \hbar I_c / 2e$ is the Josephson coupling energy. The Hamiltonian can be further written in the form of

$$H(x) = \mathbb{H}(x)\hbar w_{LC} \qquad (3.2),$$

where, $\mathbb{H}(x)$ is a dimensionless function of x given by

$$\mathbb{H}(x) = \frac{H(x)}{\hbar w_{LC}} = \left(n + \frac{1}{2}\right) - \left(\frac{J}{2p}\right)^2 b_L \cos\left\{2p\left[\frac{1}{\sqrt{2}a}\left(a^+ + a\right) + j_x\right]\right\} \qquad (3.3).$$

Here, a^+ and a are the creation and annihilation operators, $N \equiv a^+ a$ is the number operator and $J \equiv \sqrt{m w_{LC}/\hbar}$. In terms of the original SQUID device parameters

$$J^2 \equiv 2p\, R_Q / Z_0 \qquad (3.4),$$

where $R_Q \equiv h/4e^2 \approx 6.45\ \text{k}\Omega$ is the resistance quantum.

3.1.1 Cross coupling between qubit flux bias lines

The rf SQUID flux qubit is a 2nd order gradiometer which nulls out the effect of a spatially uniform magnetic field fluctuation on the qubit (See Figure 2.1). Even

though efforts were made to reduce these cross couplings at the stage of qubit design, (for example, Φ_x is applied to the qubit as a gradient field and to the compound junction as a uniform field), the cross-talk does exist between flux control lines, dc SQUID, and qubit due to the geometric layout in the qubit circuit. Table 3.1 gives the coupling matrix generated during the qubit design using Fasthenry; for instance, the mutual inductance between Φ_x and Φ_{xcjj} is $30\ \mathrm{fH}$. These cross couplings have been confirmed during the experiment. In order to precisely tune the qubit and its control circuits, steps are needed during the entire measurement to compensate for the cross couplings $\Phi_i = M_i^j I_j + \Phi_i^0 \ (i, j = m, x, xcjj)$ [68]. In a more detailed form

$$\begin{pmatrix} \Phi_m \\ \Phi_x \\ \Phi_{cjj} \end{pmatrix} = \begin{pmatrix} \frac{\partial \Phi_m}{\partial I_m} & \frac{\partial \Phi_m}{\partial I_x} & \frac{\partial \Phi_m}{\partial I_{xcjj}} \\ \frac{\partial \Phi_x}{\partial I_m} & \frac{\partial \Phi_x}{\partial I_x} & \frac{\partial \Phi_x}{\partial I_{xcjj}} \\ \frac{\partial \Phi_{xcjj}}{\partial I_m} & \frac{\partial \Phi_{xcjj}}{\partial I_x} & \frac{\partial \Phi_{xcjj}}{\partial I_{xcjj}} \end{pmatrix} \begin{pmatrix} I_m \\ I_x \\ I_{xcjj} \end{pmatrix} + \begin{pmatrix} \Phi_m^0 \\ \Phi_x^0 \\ \Phi_{xcjj}^0 \end{pmatrix} \qquad (3.5),$$

where M_i^j is a 3×3 matrix, and Φ_i^0 is the flux trapped at zero current bias.

This equation also converts current to flux thus allowing us to set the exact working conditions of the qubit and its control and readout circuits. The diagonal elements of the matrix are the inductive coupling strength between the dc SQUID magnetometer and its flux bias line, $\partial\Phi_m/\partial I_m$, the qubit and the Φ_x flux bias line, $\partial\Phi_x/\partial I_x$, and the compound junction enclosed small loop and its flux bias line, $\partial\Phi_{xcjj}/\partial I_{xcjj}$. $\partial\Phi_m/\partial I_m$ is determined by measuring the periodicity of the dc SQUID

switching distribution as a function of external flux Φ_m as displayed in Figure 2.4. Similarly, the qubit circulation current also shows a period of Φ_0 in Φ_x, from which the value of $\partial\Phi_x/\partial I_x$ can be extracted (see Figure 2.5). The coupling strength $\partial\Phi_{xcjj}/\partial I_{xcjj}$ is determined by measuring $\Phi(\Phi_x)$ as a function of Φ_{xcjj} near $\Phi_{xcjj} = \pm 0.5\,\Phi_0$. At $\Phi_{xcjj} = \pm 0.5\,\Phi_0$, the deviation between $\Phi(\Phi_x)$ and a straight line reaches a minimum value as plotted in Figure 3.1. The result is $6.30\ \mathrm{mA}/\Phi_0$. Once the diagonal elements of the coupling matrix are known, the off-diagonal elements can then be determined by monitoring the flux shifts generated by other flux bias lines.

Equation (3.5) allows us to properly compensate cross couplings so that precise control of the qubit and the read-out circuit can be obtained.

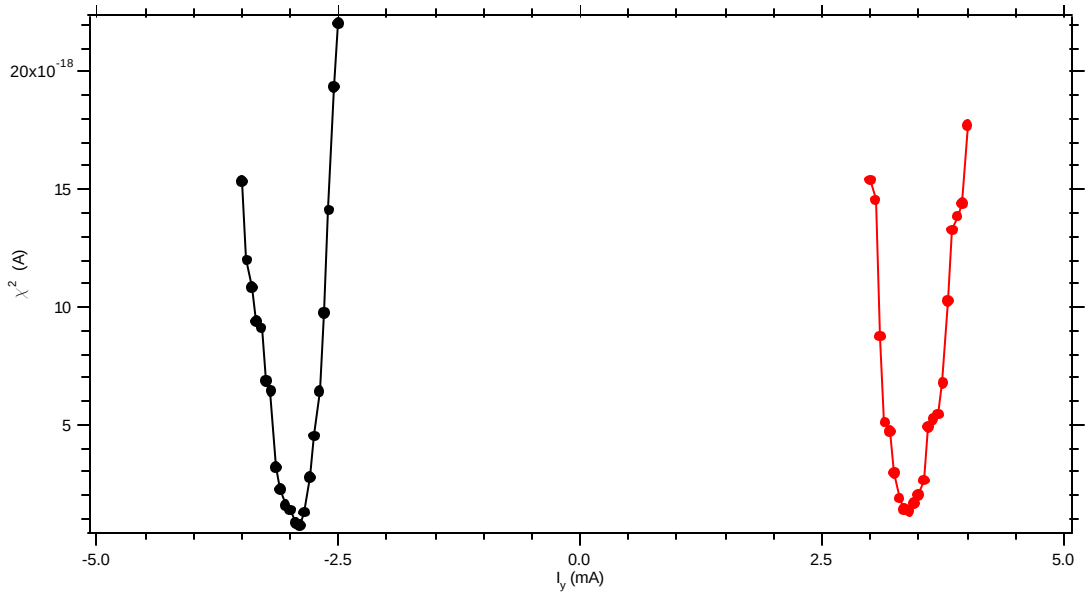

FIG. 3.1. c^2 of fitting the measured Φ vs. Φ_x data near $\Phi_{xcjj} = \pm 0.5\,\Phi_0$ to a straight line, from which $\partial I_{xcjj} / \partial \Phi_{xcjj} = 6.30\ \mathrm{mA}/\Phi_0$ was obtained.

Table 3.1. Coupling strength of qubit and its control and read-out circuits. The values in red color are the measured values.

2J (pH)	qubit	phi_x	phi_mod	dc SQUID	CPW	phi_cxjj	Qubit_cjj
qubit	1077.00	1.25/**1.09**	0.02	21.08/**23.4**	1.5/**1.38**	0.06	-
phi_x		135.57	0.02	0.03	0.08	0.03	0.00
phi_mod			51.96	2.26/**2.14**	0.01	0.01	0.00
dc SQUID				123.48	0.05	0.109/**0.182**	0.00
CPW					135.59	0.06	0.00
phi_cxjj						87.00	0.39/**0.33**
Qubit_cjj							17.79

3.1.2 Macroscopic Resonant Tunneling (MRT)

By varying the external flux, Φ_x, quantized energy levels in one of the double wells can be aligned with one of the energy levels in the opposite well, therefore the tunneling rate can be resonantly enhanced. In our experiment, the tunneling rate was obtained by measuring the transition probability as a function of Φ_x. Their relationship is given by

$$\Gamma = -\frac{\ln\left[P_s\left(\Phi_x\right)\right]}{t_{dwell}} \qquad (3.6),$$

where, P_s is the survival probability after a dwell time t_{dwell}. Figure 3.2 shows the tunneling rate as a function of Φ_x at $\Phi_{xcjj} = -0.241\,\Phi_0$. The peaks marked with arrows are where the maximum enhancement of the tunneling rate occurs, indicating approximately the position of level anticrossing. The dc SQUID records the change of occupation probability in the initial well as the system changes the fluxoid states. Figure 3.3 shows the waveforms used in the measurement of the transition probability distributions. At first, a flux bias Φ_x is applied to the qubit to initialize the system in a single well potential (e.g., the left well). Then, the flux bias is increased to V_1, where the qubit potential becomes a double well potential. The system has a finite probability to stay in the upper well after a time t_{dwell} before a short read-out pulse is applied to the dc SQUID to observe the resonant tunneling transitions. A fast read-out pulse with 10 ns rising time is applied to the dc SQUID. Its amplitude and shape are adjusted in order to distinguish two qubit states (see Figure 2.11). Each measured

point in Figure 3.2 is an average of about 10^3 events. After each event, the system is returned to its original state. The probability vs. Φ_x is measured by linearly increasing the flux bias as the energy bias e depends linearly on dj_x when $|dj_x| \ll 1$.

From the measured data, the separation between two resonant tunneling peaks, $\Delta\Phi_x = 4.977 \pm 0.018\,\mathrm{mF}_0$ is obtained.

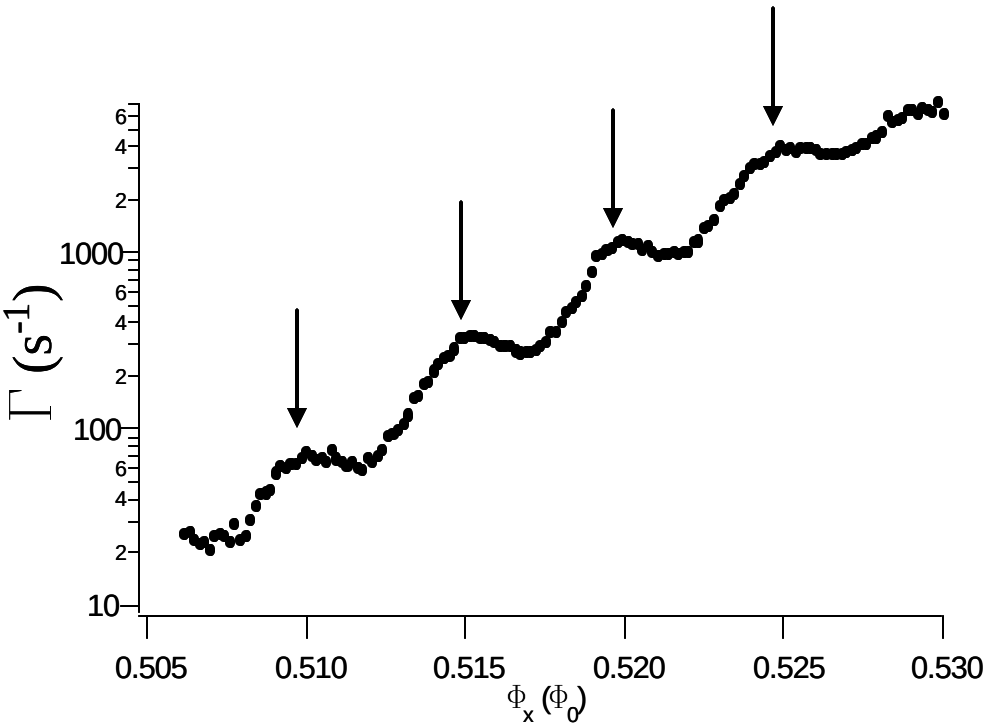

FIG. 3.2. Measured tunneling rate between two qubit states as a function of applied external flux bias Φ_x for $\Phi_{xcjj} = -0.241\,\Phi_0$ at $T = 32\,\mathrm{mK}$. The arrows indicate the positions of macroscopic resonant tunneling.

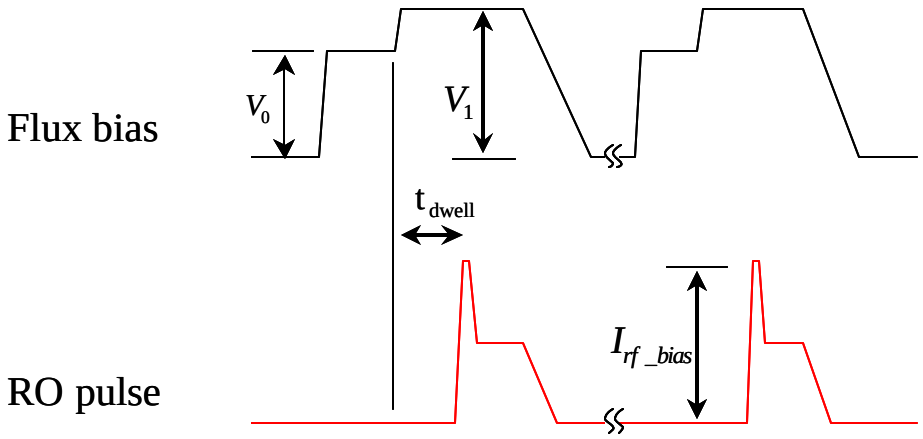

FIG. 3.3. Schematic plot of waveforms applied to the qubit to observe macroscopic resonant tunneling. t_{dwell} is the dwell time of the system in the upper well.

3.1.3 Macroscopic photon assisted tunneling (PAT)

Under the influence of a weak microwave field, a SQUID initialized in a state $|i\rangle$ can make a transition to another state $|j\rangle$ by absorbing or emitting a photon. According to Fermi's golden rule, the transition probability is given by

$$W_{i\to j}^{ph} = \frac{2p}{\hbar}\left|V_{i\to j}\right|^2 r\left(E_j - E_i \pm \hbar w_{rf}\right) \tag{3.7}$$

where, $V_{i\to j}$ is the tunneling matrix element between the states $|i\rangle$ and $|j\rangle$, and w_{rf} is the microwave frequency. In Equation (3.7) r is the density of states given by

$$r\left(\Delta E_{ji} \pm \hbar w_{rf}\right) = \frac{1}{p}\frac{\left(dE_i + dE_j\right)/2}{\left(\Delta E_{ji} \pm \hbar w_{rf}\right)^2 + \left(dE_i + dE_j\right)^2/4} \tag{3.8}$$

where, dE_i, dE_j are the linewidths of the two levels. The initial state $|i\rangle$ is the ground level in the lower well and $|j\rangle$ is an excited state in the same well. The population in the excited state can be greatly enhanced if the energy difference $\Delta E_{ji} \equiv E_j - E_i$ between the excited state and the ground state is matched to the absorbed photon energy $\hbar w_{rf}$. Consequently, the tunneling rate from the lower well

to the higher well can be significantly enhanced as the barrier seen from the excited state is reduced by ΔE_{ji}.

Experimentally, the system was initialized in the ground state of the lower potential well by waiting a sufficient time to allow the system to reach thermal equilibrium. The qubit can make a transition to the 1st excited state of the lower well by absorbing a photon with energy $\hbar w_{rf} = \Delta E_{10}$. The waveform used for measuring the occupation probability of the higher potential well with a weak microwave radiation is shown in Figure 3.4. A $1\,\mu s$ microwave pulse with a central frequency of $w_{rf}/2p = 12.21\,\text{GHz}$ was applied to the qubit before the fast readout (RO). By adjusting Φ_{xcjj} and Φ_x, the resonant condition can be achieved. Figure 3.5 is the plot of measured occupation probability of the higher well as a function of Φ_{xcjj} and Φ_x. It is clearly shown that the resonant peaks depend not only on b_{L0} and Z_0, but also on the energy scale $\hbar w_{LC}$ of the SQUID. Two useful values can be obtained from the data. One is the slope of the resonant peak position in the $\Phi_{xcjj} - \Phi_x$ plane, $\left(d\Phi_x^{PAT}/d\Phi_{xcjj}\right)$. Another is the position of the resonant peak at a fixed barrier height $b_L\left(\Phi_{xcjj}\right)$, for instance, at $\Phi_{xcjj} = 0.275\,\Phi_0$. The position of the resonant peak is $\Phi_x^{PAT} = 6.5\,\text{m}\Phi_0$ away from $0.5\,\Phi_0$.

The information obtained from the data along with the separation between the two resonant tunneling peaks described in the previous section $\Delta\Phi_x = 5.0 \pm 0.1\ \mathrm{mF}_0$ uniquely determine all SQUID parameters (except the damping resistance).

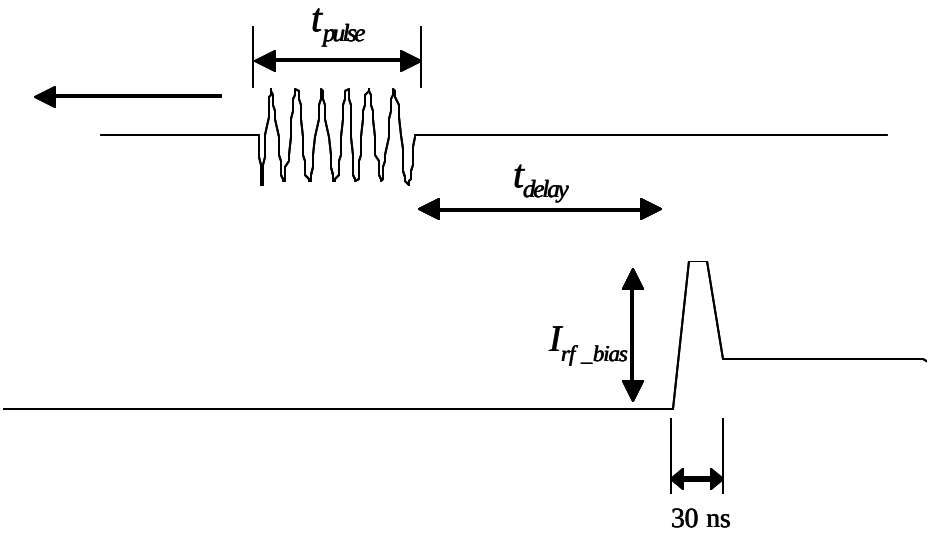

FIG. 3.4. Schematic plot of the waveform sequences applied to the qubit to observe photon assisted tunneling. Top: Microwave pulses are applied to the qubit. Bottom: A readout (RO) pulse with amplitude I_{rf_bias} is applied to the dc SQUID after the microwave pulse.

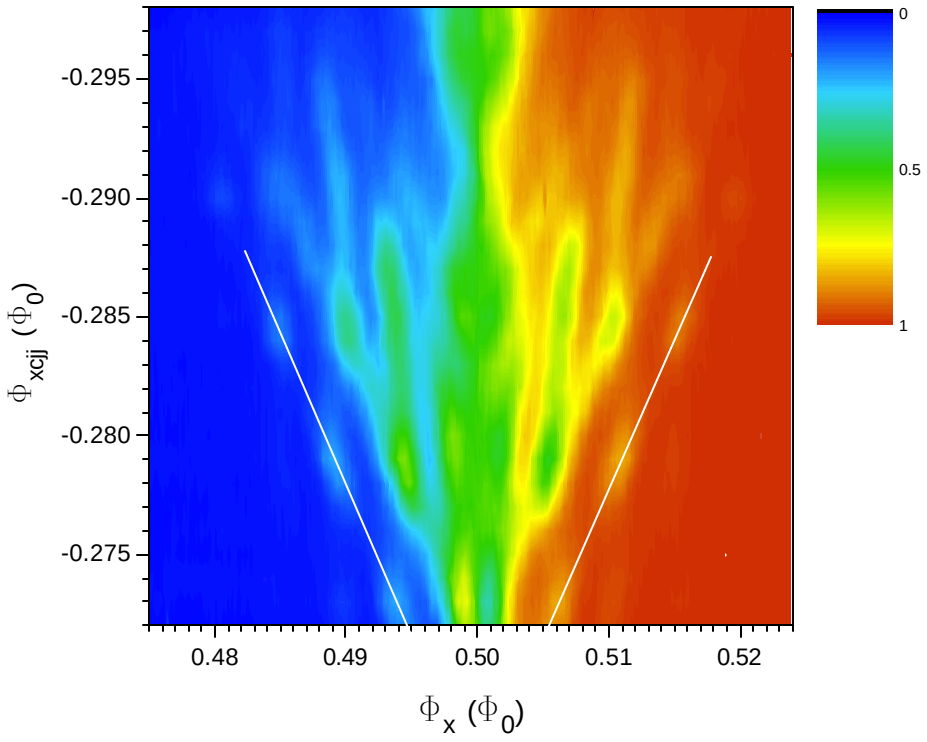

FIG. 3.5. Photon assisted tunneling in rf SQUID. The color represents the occupation probability of the higher potential well. Blue is 0 and red is 1. The microwave frequency used to excited rf SQUID is 12.21 GHz. The white lines, which are symmetric about $\Phi_x = 0.5\,\Phi_0$, mark the continuous change of the resonant peak as a function of Φ_{xcjj} and Φ_x.

3.1.4 Determination of Sample Parameters

The SQUID potential and energy level diagram are completely determined by the structure parameters, b_{L0}, Z_0, and the energy scale parameter w_{LC}. We first start from the sample parameters $L = 1088$ pH, $C = 103$ fF, $b_{L0} = 2.287$, where the value of L is obtained from the calculation of the SQUID self inductance using Fasthenry, C is estimated from the junction area and taking into account the specific capacitance of 45 fF/μm^2 for the fabrication of low J_C Nb/AlO$_x$/Nb junctions [58, 59]. This gives $Z_0 = 102.7\,\Omega$, and $w_{LC}/2p = 15.0$ GHz. When using $b_{L0} = 2.287$ and $Z_0 = 102.7\,\Omega$ to calculate the positions of resonant tunneling at energy degeneracy, the separation between two resonant tunneling peaks is about $5.0\ \mathrm{m}\Phi_0$ compared to the value of $5.0 \pm 0.1\ \mathrm{m}\Phi_0$ from the MRT data. Next, we compare the position of the calculated photon assisted tunneling peak, Φ_x^{PAT}, and its slope in the $\Phi_{xcjj} - \Phi_x$ plane to the experimental data. The calculated positions of PAT peaks are $\Phi_x = 0.489\,\Phi_0$ at $\Phi_{xcjj} = 0.267\,\Phi_0$, and $\Phi_x = 0.483\,\Phi_0$ at $\Phi_{xcjj} = 0.275\,\Phi_0$, respectively, which gives the slope of PAT peaks in the $\Phi_{xcjj} - \Phi_x$ plane of $d\Phi_x^{PAT}/d\Phi_{xcjj} = 0.799$. It is clearly shown that even the initially estimated parameters fit the MRT data well, but they don't fit the PAT data very wel. Therefore, the parameters need to be further adjusted.

The procedure is based on the fact that the positions of the PAT peaks in the $\Phi_{xcjj} - \Phi_x$ plane depend linearly on the qubit parameters b_{L0}, Z_0, and w_{LC} as these parameters vary within a small range. For example, the positions of the MRT and

PAT peaks, and the value of $z_1 \equiv d\Phi_x^{PAT} / d\Phi_{xcjj}$ were calculated for $b_{L0} = 2.25$ and $b_{L0} = 2.41$ while keeping the other two independent parameters $Z_0 = 102.7\,\Omega$, and $w_{LC}/2p = 15.0$ GHz constant. The PAT peak positions are: 1) at $\Phi_{xcjj} = 0.275\,\Phi_0$, $\Phi_x = 0.479\,\Phi_0$ for $b_{L0} = 2.25$, and $\Phi_x = 0.495\,\Phi_0$ for $b_{L0} = 2.41$; 2) at $\Phi_{xcjj} = 0.265\,\Phi_0$, $\Phi_x = 0.487\,\Phi_0$ for $b_{L0} = 2.25$, and $\Phi_x = 0.5\,\Phi_0$ for $b_{L0} = 2.41$. The values of z_1 are 0.7805 and 0.846 for $b_{L0} = 2.25$, and 2.41, respectively. Therefore, $\partial z_1 / \partial b_{L0} = 0.4094$. The b_{L0} dependent of PAT peak at $\Phi_{xcjj} = 0.275\,\Phi_0$ is $-96\,\mathrm{m}\Phi_0$. The MRT peak position at $\Phi_{xcjj} = 0.275\,\Phi_0$ also has a net change of $0.1\,\mathrm{m}\Phi_0$ when b_{L0} changes from 2.25 to 2.41. Following the same procedure for Z_0, and w_{LC}, one can repeat the calculation at $Z_0 = 99\,\Omega$, $140\,\Omega$, and $w_{LC}/2p = 14.86$ GHz, 15.57 GHz while keeping the remaining two independent parameters fixed.

The calculated parameter partial derivative matrix is listed in Table 3.2. From which, three SQUID parameters can then be obtained:

$$b_{L0} = 2.33 \pm 0.07$$

$$L = 1041 \pm 8 \text{ pH}$$

$$C = 101 \pm 5 \text{ fF}$$

The calculated MRT and PAT peak positions using the parameters derived above are in good agreement with the results obtained from the experiment. For

instance, the solid white straight line in Figure 3.5 shows the positions of the PAT peaks calculated from these SQUID parameters.

Table 3.2. The parameter partial derivative matrix calculated by varying the SQUID parameters b_{L0}, Z_0, and w_{LC} individually.

	db_{L0}	$dZ_0\ (\Omega)$	$dw_{LC}/2p\ (\mathrm{GHz})$
$\left(d\Phi_x^{MRT}\right)_{\Phi_{xcjj}=0.275\,\Phi_0}\ (\mathrm{m}\Phi_0)$	**0.50000**	**0.04892**	**0.00000**
$d\Phi_x^{PAT}/d\Phi_{xcjj}$	**0.40945**	**-0.00040**	**-0.04657**
$\left(\Phi_x^{PAT}\right)_{\Phi_{xcjj}=0.275\,\Phi_0}$	**-96.00000**	**0.09620**	**-11.51344**

3.2 Inter-well Energy Relaxation Time in rf SQUID

3.2.1 Inter-well Energy Relaxation Time

In principle, quantum computation requires the qubit to remain coherent during the gate operation. On the other hand, the qubit, in practice, is not an isolated system [69]. The qubit state needs to be prepared and controlled in experiments, and it inherently interacts with various degrees of freedom. For example, the rf SQUID flux qubit interacts with flux control lines and the dc SQUID. In each operation cycle, the coherent superposition of qubit states will be destroyed after the signal is detected by the dc SQUID [16, 18, 43, 70]. It is extremely important to understand the decoherence mechanisms. A recent study shows that the energy relaxation is the dominant source of decoherence in an rf SQUID; in particular, $g_1 \simeq 2g_2$ [70], where, g_1 is the energy relaxation rate, and g_2 is the dephasing rate. As the inter-well relaxation time is one of the fundamental measures of a qubit's quality, it is important to understand its mechanism in our system.

Our approach to studying the in-well relaxation time is based on a free decay following the microwave pumping process as depicted in Figure 3.6. The barrier height ΔU and the energy bias e of the double well potential are adjusted *in situ* so that under the barrier there are two energy levels in the lower well and one energy level in the upper well. For each measurement cycle, the qubit is initially prepared in the ground state of the lower-well. When applying a microwave pulse with duration of t_{pulse}, if the microwave frequency matches the energy difference between the initial

state and one of the states in the upper-well, the system has a finite probability of being excited directly into this upper-well state. The transition between the qubit double-well potential results in a change in the qubit's circulation current which can be detected by the dc SQUID [16]. After the microwave source was turned off, we wait a period of time t_{delay} to allow the qubit to relax from the upper-well ground state to the lower-well. We denote the relaxation rate from the upper-well ground state to the 1st excited state of the lower well as g_{21} and the in-well energy relaxation rate from the 1st excited state of the lower well to the ground state as g_{10} [17, 18, 71]. It is easy to show that the probability of finding the system remaining in the upper-well is given by

$$P_1(t) = a \exp\left[-(g_{21} + g_{20})t\right] \qquad (3.9),$$

where, g_{20} denotes the relaxation rate from the upper well ground state directly to the lower well ground state.

The fast current bias pulse of amplitude I_{rf_bias} and pulse length 30 ns (the rising/falling time of the pulse is 10 ns) followed by a trailing plateau of 10 μs (Figure 3.4) is applied to the dc SQUID via a cryogenic coaxial cable of 100 MHz. The amplitude and the duration of the fast current bias pulse are optimized to distinguish two qubit states as discussed in the previous chapter.

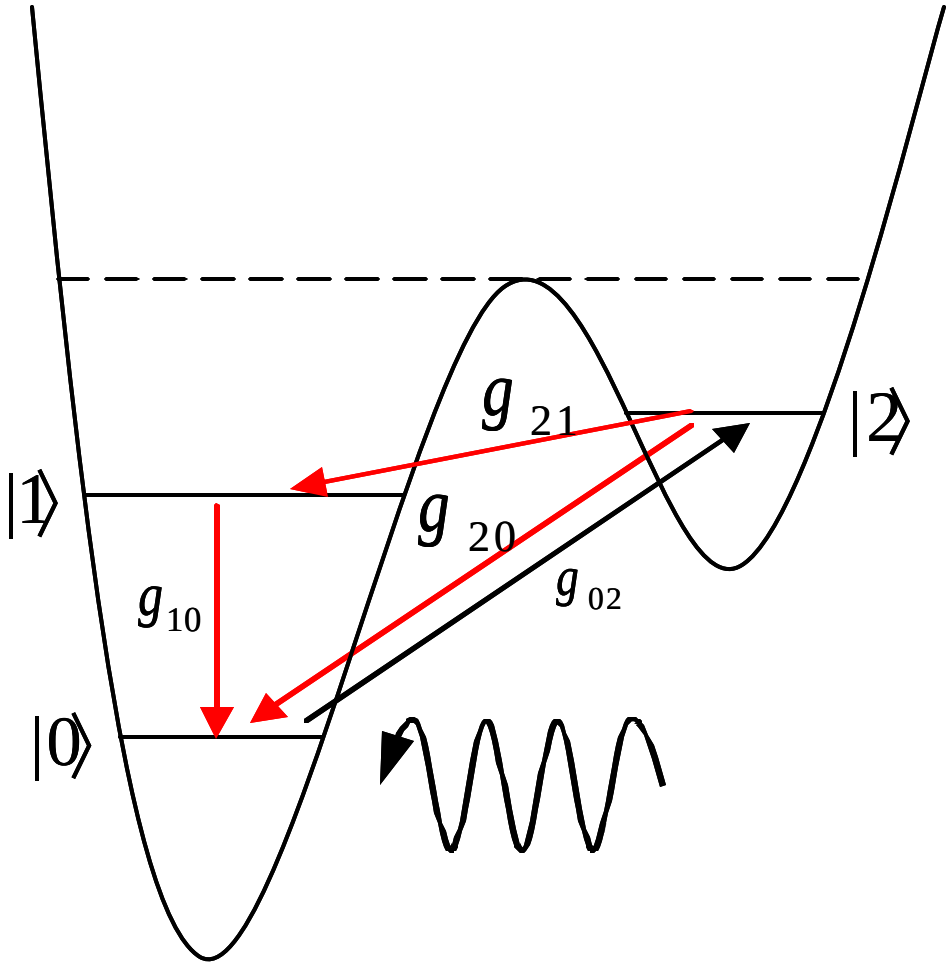

FIG. 3.6. Schematic drawing of the qubit's double-well potential and the first three energy levels. The qubit decays first from the upper-well ground state to the lower-well's 1st excited state after the microwaves were turned off with a rate g_{21}, followed by decaying to the lower-well ground state with a rate g_{10}.

Figure 3.7 shows the calculated energy level diagram of the SQUID qubit at $\Phi_{xcjj} = 0.303\,\Phi_0$ where energy is measured with respect to the ground state of the lower well. The dashed line is the calculated energy barrier of the double-well potential. Energy levels below the barrier are localized while those above it are delocalized. The dotted line represents a photon energy of $w_{rf}/2p = 12.75$ GHz. At values of Φ_x indicated by the arrows, the system can absorb a photon which results in an inter-well transition.

An example of the upper-well occupation probability P_1 as a function of delay time t_{delay} between the falling edge of the microwave pulse and the rising edge of RO pulse is shown in Figure 3.8. The data were taken at values of $\Phi_{xcjj} = 0.303\,\Phi_0$ and $\Phi_x = \Phi_0/2 + 5.47$ mF $_0$. The data clearly shows an exponential decay as described by Equation (3.9). When the rate g_{21} is much greater than g_{20}, g_{21} dominates the relaxation process and Equation (3.9) can be reduced to

$$P_1(t) = a\exp\left(-g_{21}^{*}t\right) \qquad (3.10).$$

Therefore, the inter-well energy relaxation time $\left(g_{21}^{*}\right)^{-1} = 3.64 \pm 0.04\ \mu s$, is obtained by fitting the experimental data to the simple exponential form of Equation (3.10).

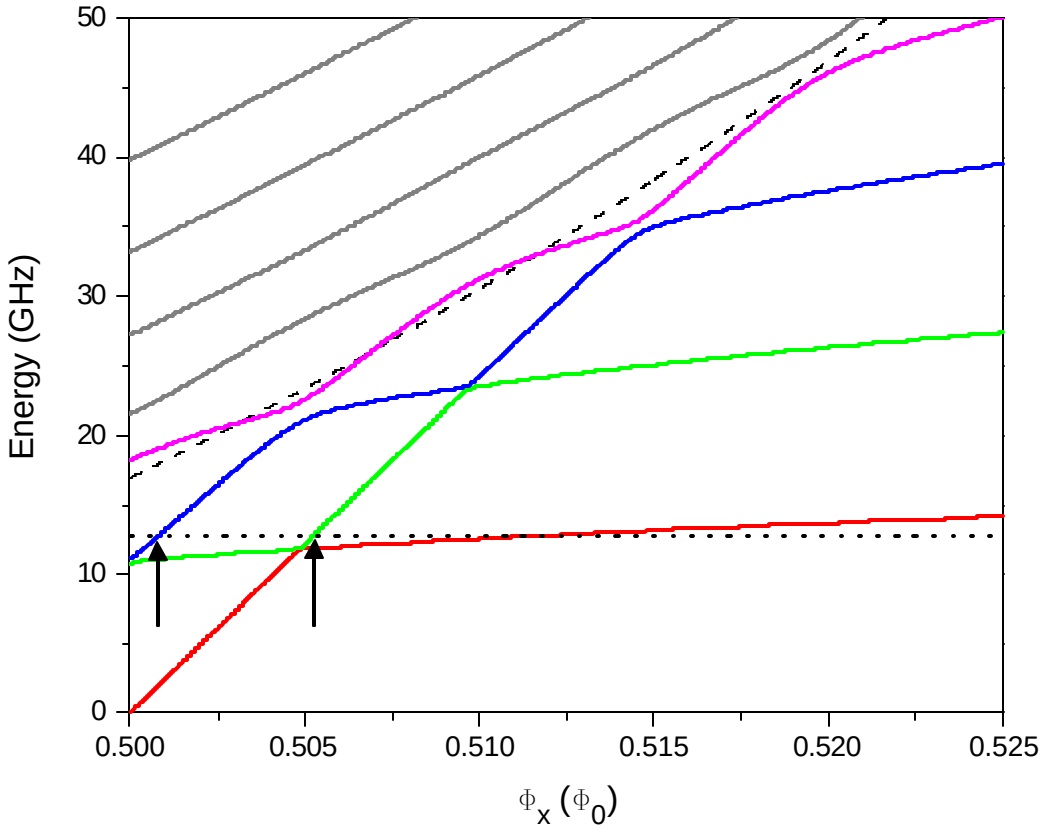

FIG. 3.7. Solid color lines are the calculated energy levels for upper (diagonals) wells and lower (horizontals) wells with respect to the zeroth level of the lower-well at $\Phi_{xcjj} = 0.303\,\Phi_0$. The dashed black line is the top of the energy barrier. Arrows mark the photon (dotted line, $w_{rf}/2p = 12.75$ GHz) absorption resonances with energy levels of the opposite well.

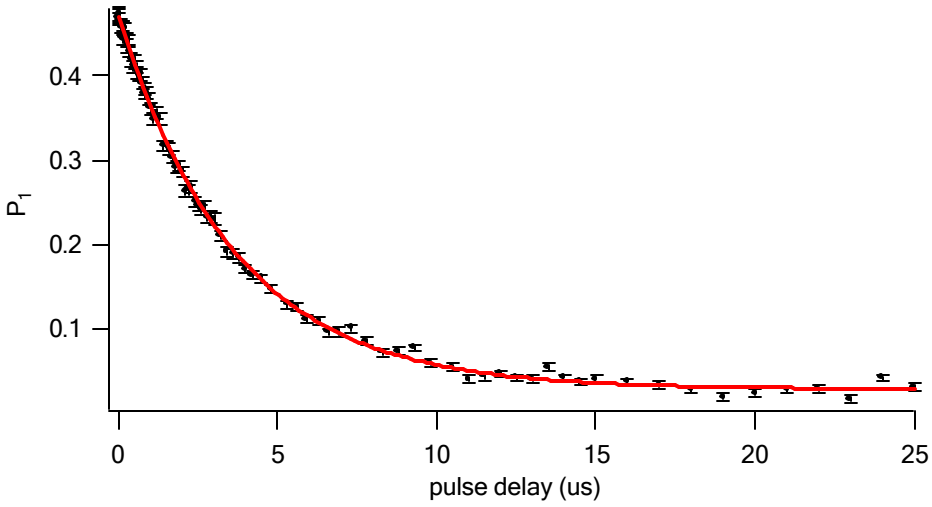

FIG. 3.8. Measured upper-well occupation probability as a function of t_{delay} for $\Phi_{xcjj} = 0.303\,\Phi_0$, $(\Phi_x - 0.5\,\Phi_0) = 5.47\,\mathrm{mF}_0$. The red curve is the best fit to an exponential with time constant of $3.64 \pm 0.04\,\mu\mathrm{s}$.

3.2.2 Effective Damping Resistance

It is well known that both the energy relaxation time $T_1 \equiv g_1^{-1}$ and the dephasing time $T_2 \equiv g_2^{-1}$ lead to decoherence. In rf SQUID qubits, T_1 and T_2 are inversely proportional to the level of dissipation [72]:

$$g_{21}^{*} = \frac{2p\Delta E_{21}}{\hbar}\frac{R_Q}{R_{eff}}\left(1+\coth\left(\frac{\Delta E_{21}}{2k_BT}\right)\right)\left|X_{21}\right|^2 \qquad (3.11),$$

where, R_{eff} is the effective damping resistance of the qubit and $X_{ij} = \langle i|\Phi|j\rangle/\Phi_0$ is the reduced tunneling matrix element. Using the measured inter-well relaxation time $\left(g_{21}^{*}\right)^{-1} = 3.64 \pm 0.04\ ms$ along with the applied microwave frequency of $w_{rf}/2p = 12.75$ GHz. The qubit depicted in Figure 3.8 at $\Phi_x = \Phi_0/2 + 5.47$ mF $_0$ and $\Phi_{xcjj} = 0.303\ \Phi_0$ has

$$\Delta E_{10}/h = 11.04 \text{ GHz},\ \Delta E_{20}/h = 12.75 \text{ GHz},\ \Delta E_{21}/h = 1.71 \text{ GHz}$$

$$X_{10} = 4.00\times10^{-2},\ X_{20} = 8.55\times10^{-4},\ X_{21} = 7.96\times10^{-3}.$$

The effective damping resistance of $R_{eff} = 200$ kΩ is obtained, which is more than 10^3 times lower than the measured quasiparticle resistance of cofabricated junctions [59].

With the knowledge of the effective damping resistance of the qubit, $\Delta E_{10}/h = 11.04$ GHz and $X_{10} = 4.00\times10^{-2}$, we obtain the value of the in-well energy relaxation time to be $T_1 = g_{10}^{-1} \simeq 22$ ns.

3.3 Quantum Three-Level System

3.3.1 Introduction

Superconducting qubits based on the Josephson devices, including phase qubit (Josephson junction) [49], the flux qubit (SQUID) [49, 73, 74], and charge qubit (Cooper pair box) [75, 76] have advantages over other qubit candidates, such as trapped ions [77], nuclear spin [78], and cavity QED [79] in that:

1) Their states can readily be prepared and controlled [49];
2) They can be scaled up to form quantum circuits and networks [69];
3) It is relatively straightforward to address a single qubit and make single-shot state readout.

On the other hand, superconducting qubits have multiple energy levels. The noncomputational states are not well separated from the two computational states, which can cause significant errors during the quantum gate operation.

In order to address this problem, a Λ-shaped three-level rf SQUID qubit has recently been introduced [48]. The basic idea is to use an auxiliary level $|a\rangle$ to facilitate gate operation while reducing the error rate. When compared to other types of commonly used solid state two-level qubits the Λ-shaped three-level rf SQUID qubit has higher quantum quality factor (i.e., the ratio between decoherence time and gate time).

3.3.2 Dynamics of Quantum Three level system

In the incoherent regime, the temporal evolution of a Λ-shaped three-level rf SQUID qubit as depicted in Figure 3.6 can be described by a general master equation

$$\frac{dr_0}{dt} = g_{00} r_0 + g_{01} r_1 + g_{02} r_2, \tag{3.12a}$$

$$\frac{dr_1}{dt} = g_{10} r_0 + g_{11} r_1 + g_{12} r_2, \tag{3.12b}$$

$$\frac{dr_2}{dt} = g_{20} r_0 + g_{21} r_1 + g_{22} r_2, \tag{3.12c}$$

where, g_{ij} for $i, j = 0, 1, 2$ are transition rates between relevant levels and r_k for $k = 0, 1, 2$ are the occupation probabilities of levels $|0\rangle$, $|1\rangle$, and $|2\rangle$.

For the three-level rf SQUID qubit, the master equation can be rewritten as

$$\frac{dr_0}{dt} = -g_{02} r_0 + g_{10} r_1 + (g_{21} + g_1) r_2 \tag{3.13a},$$

$$\frac{dr_1}{dt} = g_{21} r_2 - g_{10} r_1 \tag{3.13b},$$

$$\frac{dr_2}{dt} = g_{02} r_0 - g_{21} r_2 - (g_{20} + g_1) r_2 \tag{3.13c},$$

where, g_{02} is the stimulated excitation rate from $|0\rangle$ to $|2\rangle$. At time $t = 0$, the system is initialized at the ground state in the lower well $|0\rangle$, therefore $r_0(0) = 1$, and $r_1(0) = r_2(0) = 0$. The occupation probabilities r_0, r_1, and r_2 satisfy

$$r_0 + r_1 + r_2 \equiv 1 \tag{3.14}.$$

When microwaves are turned off after the system reaches the steady state, the system starts its free decay with spontaneous decay rate g_{20} from $|2\rangle$ to $|0\rangle$, g_{21} from $|2\rangle$ to $|1\rangle$, and intra-well relaxation rate of g_{10} from $|1\rangle$ to $|0\rangle$. As from Equation (3.14), only two of the three population r_0, r_1, and r_1 are independent variables. The master equation can be reduced to

$$\frac{dr_0}{dt} = (g_{00} - g_{02})\, r_0 + (g_{01} - g_{02})\, r_1 + g_{02} \qquad (3.15a),$$

$$\frac{dr_1}{dt} = (g_{10} - g_{12})\, r_0 + (g_{11} - g_{12})\, r_1 + g_{12} \qquad (3.15b).$$

Generally, for a given system, the stimulated excitation rate is proportional to the applied microwave power $g_{02} = aP_{rf}$ under the condition of weak microwave fields, according to Fermi's golden rule. The master equation (3.15a and 3.15b) can be solved analytically

$$r_0(t) = A_0 \exp(-\Gamma_1 t) + B_0 \exp(-\Gamma_2 t) \qquad (3.16a),$$

$$r_1(t) = A_1 \exp(-\Gamma_1 t) + B_1 \exp(-\Gamma_2 t) \qquad (3.16b),$$

where, A_0, A_1, B_0, and B_1 are constants. The occupation probability shows double exponential decay with decay rates:

$$\Gamma_1 = \frac{1}{2}\left\{(2g_{02} + g_{10} + g_{20} + g_{21}) - \left[(2g_{02} + g_{20} + g_{21} - g_{10})^2 - 4g_{02}g_{21}\right]^{1/2}\right\} \qquad (3.17a),$$

$$\Gamma_2 = \frac{1}{2}\left\{(2g_{02} + g_{10} + g_{20} + g_{21}) + \left[(2g_{02} + g_{20} + g_{21} - g_{10})^2 - 4g_{02}g_{21}\right]^{1/2}\right\} \qquad (3.17b),$$

The complete derivation of the solution is presented in Appendix B (Dynamics of quantum three-level system). It is clear that if $A_0 > B_0$ ($A_1 > B_1$) and the two decay rates are real, the amplitude of the slow decay term is larger than that of the fast decay term. Therefore, the slow exponential decay term (first term) will be left in the solutions (Equation 3.16a and 3.16b).

3.3.3 Calibration of microwave-to-qubit coupling strength

The dynamics of the three-level system provides us a unique method to determine the microwave-to-qubit coupling. It is important to have an accurate knowledge for precise qubit state control using microwave pulses.

The experimental procedure is similar to that of the PAT experiment. The system is initialized in the ground state of the lower potential well by waiting a long enough time. The system is placed in one of the levels in the upper well by absorbing a photon. The waveforms sequences for the measurement of the transition probability under weak microwave radiation are depicted in Figure 3.4. A 100 ns microwave pulse of with a central frequency of $w_{rf}/2p = 12.75$ GHz is applied to the qubit right before the fast RO pulse is applied. The upper-well occupation probability, P_1, as a function of microwave pulse duration, t_{pulse}, is recorded as shown in Figure 3.9 at $\Phi_{xcjj} = 0.303\,\Phi_0$ and $\Phi_x = \Phi_0/2 + 5.47\ \mathrm{mF}_0$. By varying the microwave power, we can plot the upper well state excitation rate as a function of the applied microwave power.

Once we plug into Equation (3.17a) the values of the corresponding transition rates calculated using the SQUID parameters fitted to the upper well excitation rate versus the microwave power (Figure 3.10), the microwave-to-qubit coupling strength $a = 24.9 \pm 1.1$ MHz/mW is obtained.

3.4 Discussion

From the resonant tunneling and spectroscopy, we found the line width of the resonant peaks is about 3 mΦ_0. Both inhomogeneous broadening and the intrinsic dephasing may cause this line width. The dephasing time inferred from the line width is about 0.1 ns. This indicated that the dissipation of the rf SQUID is large and the decoherence time is very short. Therefore, we could not observe coherent quantum phenomenon. The inferred in-well energy relaxation time, which is an independent parameter of an rf qubit, is also one of the decoherence sources. The measuring of microwave-to-qubit coupling strength in a three-level setup provides us a unique method for precise control of the qubit state using microwave.

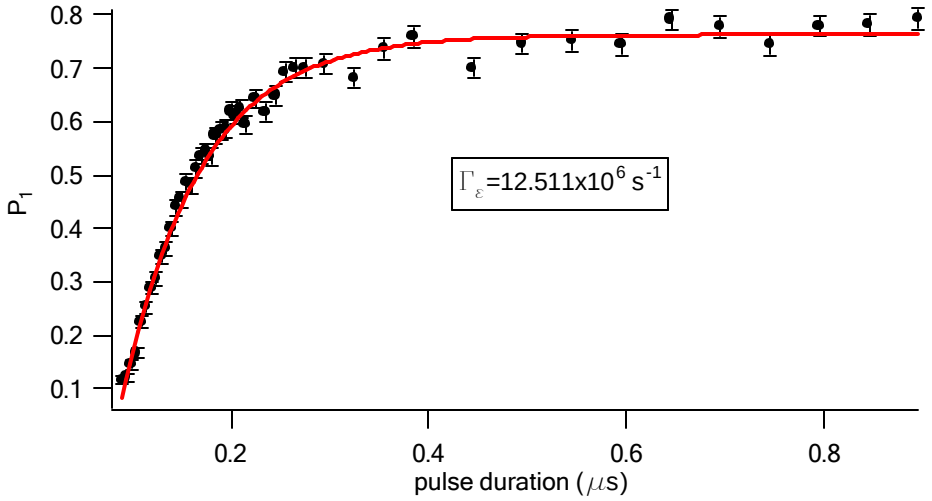

FIG. 3.9. Example of measuring the upper-well excitation rate by fitting the upper-well occupation probability as a function of microwave pulse duration t_{pulse} for $\Phi_{xcjj} = 0.303\ \Phi_0$, $\left(\Phi_x - 0.5\Phi_0\right) = 5.47\ \mathrm{m}\Phi_0$.

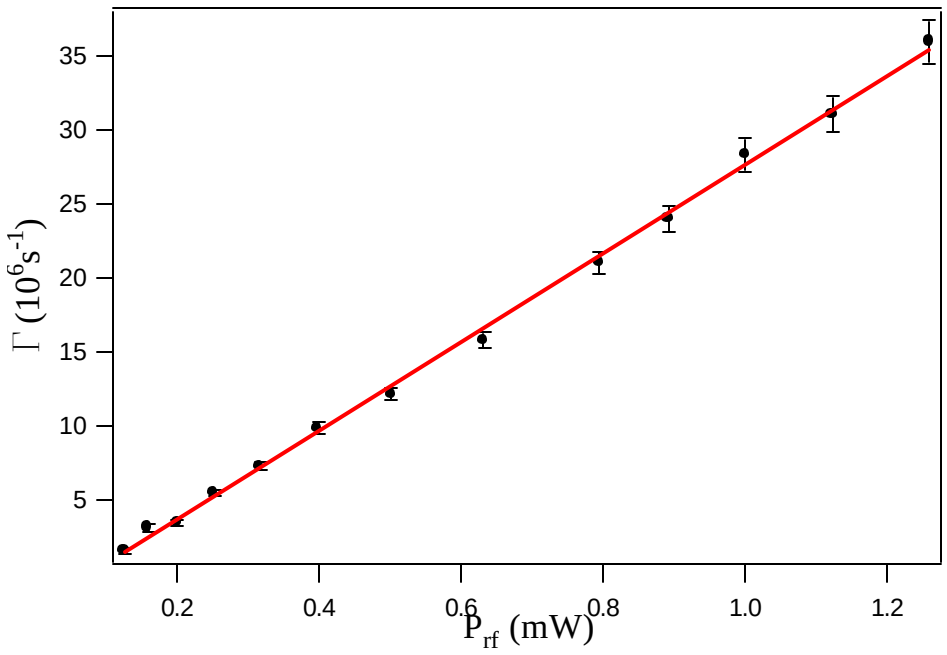

FIG. 3.10. Plot of upper-well excitation rate as a function of applied microwave power for $\Phi_{xcjj} = 0.303\,\Phi_0$, $(\Phi_x - 0.5\Phi_0) = 5.47\,\mathrm{m}\Phi_0$.

Chapter 4. Flux noise in SQUID qubit

Superconducting qubits based on Josephson junction have the advantages that they can be scaled up and their quantum states are easy to prepare and control. Rabi oscillations have been demonstrated in various quantum circuits [18-22, 80], which make the superconducting qubits promising for implementing quantum computing [69]. However, coherence can be destroyed by decoherence such as dephasing and energy relaxation [49] due to the strong interactions between the macroscopic variables and the many degrees of freedom from the environment. A few microseconds coherence time have been achieved in several experiments using superconducting qubits, which are close to realize the quantum computing ($> 10\ \mu s$). Several mechanisms of decoherence, such as background charge fluctuation [53], bias flux fluctuation [52, 53, 55, 81], critical current fluctuation [52], thermal fluctuations of photon numbers [82], the dielectric loss from two level fluctuators coupled to qubit [51], have been discussed and the list is still expanding. Unfortunately, the limited understanding of the mechanisms of decoherence is still a major challenge to the use of superconducting qubits for scalable quantum computation. To identify the sources of decoherence and to further increase coherence time are two of the crucial tasks of superconducting qubits research. In this chapter, I will present evidence which shows that the integrated low frequency flux noise increase linearly with the inductance of the flux qubits.

4.1 Models of 1/f Flux noise

Recently, several theoretical models of low frequency flux noise have been proposed [54, 83, 84]. For example, Koch *et al* [54] developed a model of low frequency flux noise using a flux qubit whose configuration contains a superconducting loop. In their model, decoherence is caused by unpaired electrons trapped in defects where their spins have fixed, random orientations. An electron can be trapped by a defect for a long period of time with the direction of its spin remaining unchanged at low temperature [85] due to spin-orbit coupling [86].

To estimate the low frequency flux noise using Koch's model, we first assume that the defects with density of n are uniformly distributed over the SQUID sample with inner and outer dimensions of $2d$, $2D$ and loop width W (Figure 4.1). Three regions were defined: the superconducting loop, the exterior region, and the hole region that is enclosed by the SQUID loop. A small current loop was used to simulate mutual inductance $M(x,y)$ between electron's magnetic moment and the SQUID loop. The loop area of A had a current i flowing in it so that $A \cdot i = m_B$, where $m_B = 9.27\times10^{-24}$ J/T is the Bohr magneton. The flux per Bohr magneton coupled into the SQUID loop has been calculated, $\Phi_0/m_B = M(x,y)/A$, and the total mean square normalized flux noise from three regions coupled into the SQUID is obtained:

$$\left\langle \left(d\Phi_{st}\right)^2 \right\rangle = 8nm_B^2 \int_0^{L+D} dx \int_0^{x} dy \left[M(x,y)/A \right]^2 \qquad (4.1),$$

where, L_d is the distance beyond the SQUID loop in the integration. For reasons of simplicity, we take the upper limit of $M(x,y)$ to be 1 $n\Phi_0/m_B$ and the range of integration from 10^{-4} Hz to 10^9 Hz during our calculation. The $1/f$ spectral density of the flux noise is given by

$$\frac{S_\Phi(f)}{\Phi_0^2} \approx \frac{\left\langle \left(d\Phi_{st}/\Phi_0\right)^2 \right\rangle}{30f} \tag{4.2}$$

Notice that this model predicts that the magnitude of the rms (root mean square) flux noise depends not on the total area of the SQUID but on the ratio of the linear dimension of the SQUID for constant aspect ratio D/W.

Instead of the $1/f$ flux noise caused by unpaired electron-trapping as described in Koch's model, Sousa's proposal of the magnetic flux noise is due to the spin-flips of paramagnetic dangling-bonds at the amorphous-semiconductor/oxide interface [84]. The dangling-bond forms the trapping center near the Fermi energy ($e_F \pm k_B T$) for interface conduction electrons with spin-flips due to the interactions with the local structural defects at the interface, for example, Si/SiO_2 and other amorphous oxide interfaces that are used as the substrate for superconducting qubits. The corresponding noise also has a $1/f$ frequency dependent. In contrary to Sousa's model, Bialczak *et al* [83] claimed that the measured flux noise should be interpreted by the defects at the Si/SiO_x interface since their devices were made on sapphire substrates.

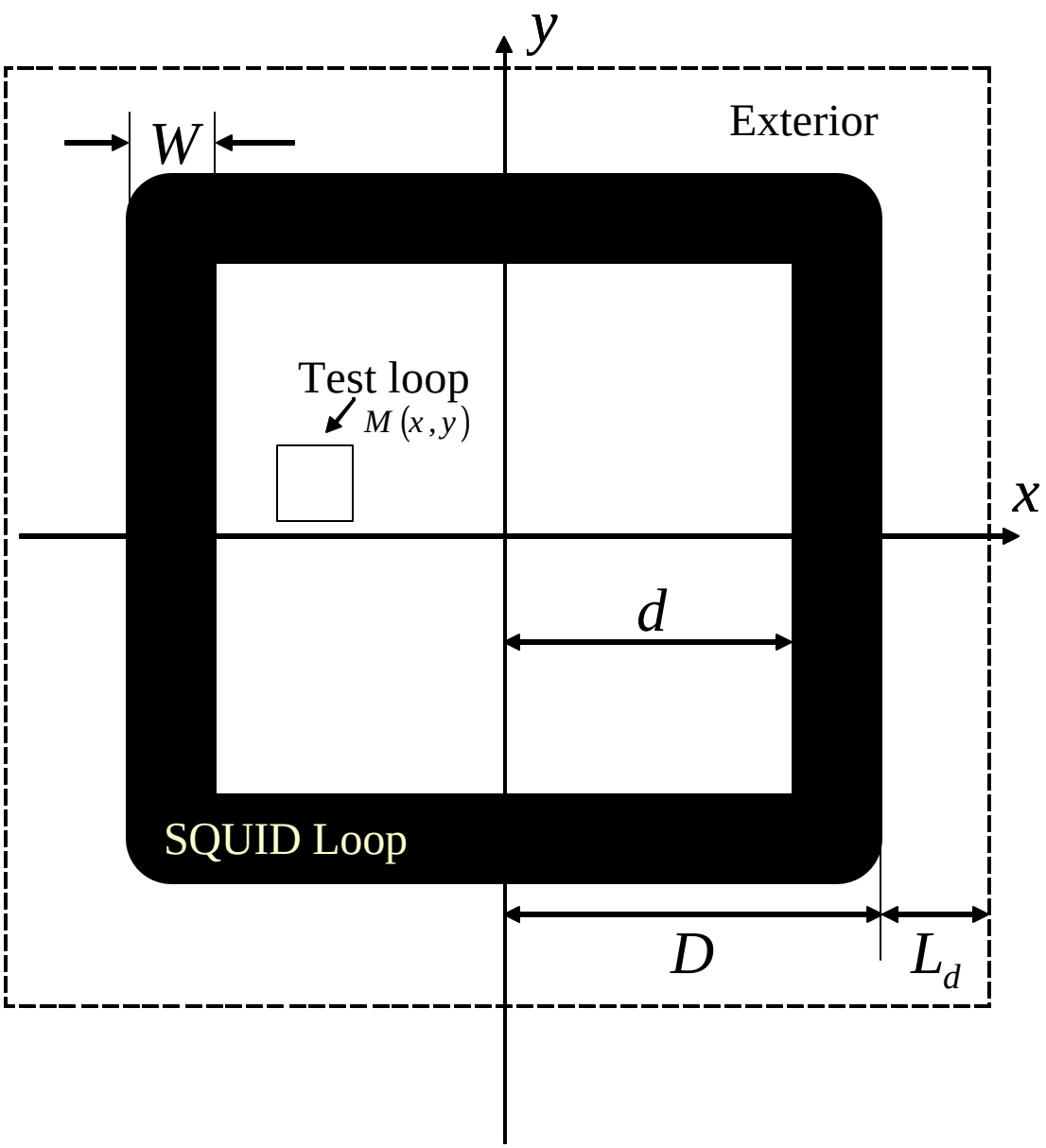

Fig. 4.1. Configuration of SQUID loop and test current loop that coupled to the SQUID and moved along the x-axis.

4.2 Discussion

The magnitude of the flux noise can be obtained from MRT and/or PAT peak by fitting the data to a Gaussian function. The standard deviation of the Gaussian then equals to the root-mean-square of flux noise. It can be seen that flux noise extracted from four qubits with various self inductances (sizes) shows a good linear dependent of the qubit self inductance as plotted in Figure 4.2 for four different qubit samples. Although the linear dependence of flux noise on qubit inductance agrees with that predicted by [54], the measured flux noise of $0.93\,\mathrm{m}\Phi_0$ on sample VJKQC4-40-3 needs a defect density that is about 10^2 greater than the value used in [54]. The difference is so great which unlikely can be explained by any existing models. Therefore, our result suggests that the observed low frequency flux noise may very well arise from a yet unknown mechanism. Moreover, the long decoherence times reported so far have been achieved in NbN- and Al-based qubits [18, 21, 22, 51, 54, 70, 80, 81, 87-89]. Based on our result, which corresponds to a decoherence time of $T_2^* < 1\,\mathrm{ns}$, we conclude that the unexpectedly strong low frequency flux noise is responsible for not being able to observe coherent oscillation between different fluxoid states in Nb-based large inductance flux qubit [71]. Hence, for implementing quantum computation with superconducting flux qubits it is imperative to understand the microscopic mechanism of low frequency flux noise.

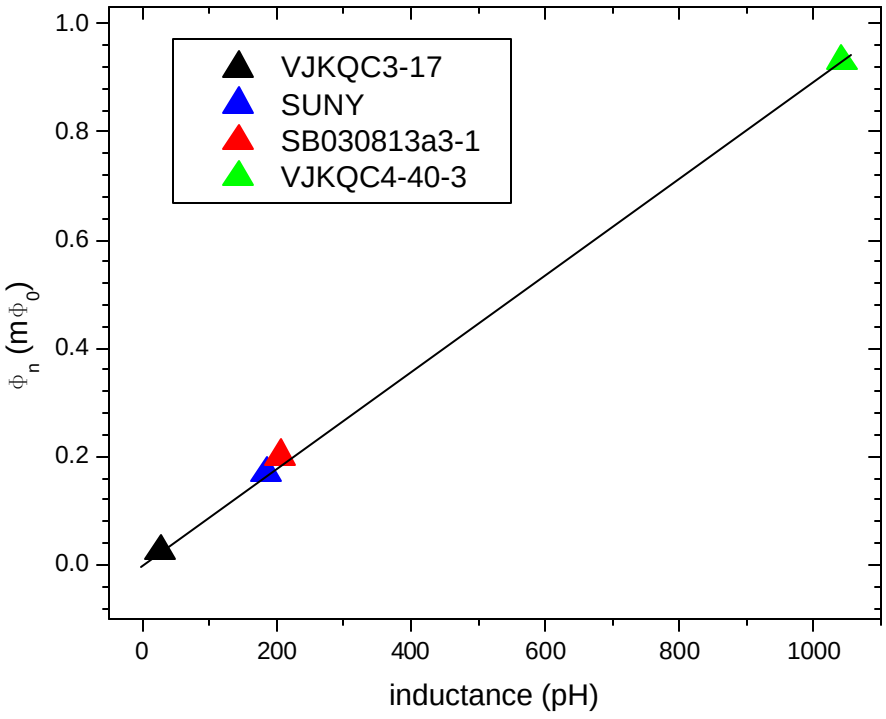

Fig. 4.2. Measured flux noise in SQUIDs for four different qubit samples with different qubit self inductance.

References

1. Caldeira, A.O. and A.J. Leggett, *Influence of Dissipation on Quantum Tunneling in Macroscopic Systems.* Physical Review Letters, 1981. **46**(4): p. 211.
2. Leggett, A.J., et al., *Dynamics of the dissipative two-state system.* Reviews of Modern Physics, 1987. **59**(1): p. 1.
3. Leggett, A.J. and A. Garg, *Quantum mechanics versus macroscopic realism: Is the flux there when nobody looks?* Physical Review Letters, 1985. **54**(9): p. 857.
4. Clarke, J., et al., *Quantum Mechanics of a Macroscopic Variable: The Phase Difference of a Josephson Junction.* Science, 1988. **239**(4843): p. 992-997.
5. Devoret, M.H., J.M. Martinis, and J. Clarke, *Measurements of Macroscopic Quantum Tunneling out of the Zero-Voltage State of a Current-Biased Josephson Junction.* Physical Review Letters, 1985. **55**(18): p. 1908.
6. Schwartz, D.B., et al., *Quantitative Study of the Effect of the Environment on Macroscopic Quantum Tunneling.* Physical Review Letters, 1985. **55**(15): p. 1547.
7. Voss, R.F. and R.A. Webb, *Macroscopic Quantum Tunneling in 1-mum Nb Josephson Junctions.* Physical Review Letters, 1981. **47**(4): p. 265.
8. Washburn, S., et al., *Effects of Dissipation and Temperature on Macroscopic Quantum Tunneling.* Physical Review Letters, 1985. **54**(25): p. 2712.
9. Martinis, J.M., M.H. Devoret, and J. Clarke, *Energy-Level Quantization in the Zero-Voltage State of a Current-Biased Josephson Junction.* Physical Review Letters, 1985. **55**(15): p. 1543.
10. Rouse, R., S. Han, and J.E. Lukens, *Observation of Resonant Tunneling between Macroscopically Distinct Quantum Levels.* Physical Review Letters, 1995. **75**(8): p. 1614.
11. Silvestrini, P., et al., *Observation of Energy Levels Quantization in Underdamped Josephson Junctions above the Classical-Quantum Regime Crossover Temperature.* Physical Review Letters, 1997. **79**(16): p. 3046.
12. Han, S., J. Lapointe, and J.E. Lukens, *Observation of incoherent relaxation by tunneling in a macroscopic two-state system.* Physical Review Letters, 1991. **66**(6): p. 810.
13. Han, S., R. Rouse, and J.E. Lukens, *Generation of a Population Inversion between Quantum States of a Macroscopic Variable.* Physical Review Letters, 1996. **76**(18): p. 3404.
14. Han, S., R. Rouse, and J.E. Lukens, *Observation of Cascaded Two-Photon-Induced Transitions between Fluxoid States of a SQUID.* Physical Review Letters, 2000. **84**(6): p. 1300.

15. S. Han, J.L., and J. E. Lukens, *Single-Electron Tunneling and Mesoscopic Devices*, ed. (Springer-Verlag, Berlin, Heidelberg, 1991). Vol. 31, pp. 219-222.
16. Friedman, J.R., et al., *Quantum superposition of distinct macroscopic states.* Nature, 2000. **406**(6791): p. 43-46.
17. van der Wal, C.H., et al., *Quantum Superposition of Macroscopic Persistent-Current States.* Science, 2000. **290**(5492): p. 773-777.
18. Chiorescu, I., et al., *Coherent Quantum Dynamics of a Superconducting Flux Qubit.* Science, 2003. **299**(5614): p. 1869-1871.
19. Martinis, J.M., et al., *Rabi Oscillations in a Large Josephson-Junction Qubit.* Physical Review Letters, 2002. **89**(11): p. 117901.
20. Nakamura, Y., Y.A. Pashkin, and J.S. Tsai, *Coherent control of macroscopic quantum states in a single-Cooper-pair box.* Nature, 1999. **398**(6730): p. 786-788.
21. Vion, D., et al., *Manipulating the Quantum State of an Electrical Circuit.* Science, 2002. **296**(5569): p. 886-889.
22. Yu, Y., et al., *Coherent Temporal Oscillations of Macroscopic Quantum States in a Josephson Junction.* Science, 2002. **296**(5569): p. 889-892.
23. Onnes, H.K., Comm. Phys. Lab. Univ. Leiden, Nos., 1911. **119, 120, 122**.
24. Abrikosov, A.A., Sov. Phys. JETP, 1957. **5, 1174**.
25. Bardeen, J., L.N. Cooper, and J.R. Schrieffer, *Theory of Superconductivity.* Physical Review, 1957. **108**(5): p. 1175.
26. Ginzburg, V.L. and L.D. Landau, *On the theory of superconductivity.* Zh. Eksp. Teor. Fiz., 1950. **20**: p. 1064-1082.
27. London, F. and H. London, *Supraleitung und diamagnetismus.* Physica, 1935. **2**(1-12): p. 341-354.
28. Maxwell, E., *Isotope Effect in the Superconductivity of Mercury.* Physical Review, 1950. **78**(4): p. 477.
29. Meissner, W. and R. Ochsenfeld, *Ein neuer Effekt bei Eintritt der Supraleitfähigkeit.* Naturwissenschaften, 1933. **21**(44): p. 787-788.
30. Reynolds, C.A., et al., *Superconductivity of Isotopes of Mercury.* Physical Review, 1950. **78**(4): p. 487.
31. Josephson, B.D., *Possible new effects in superconductive tunnelling.* Physics Letters, 1962. **1**(7): p. 251-253.
32. Barone, A. and G. Paterno, *Physics and Applications of the Josephson Effect*. 1982.
33. Stewart, W.C., *Current-Voltage Characteristic of Josephson junctions.* Applied Physics Letters, 1968. **12**(8): p. 277-280.
34. Deutsch, D., A. Barenco, and A. Ekert, *Universality in Quantum Computation.* Proceedings of the Royal Society: Mathematical and Physical Sciences (1990-1995), 1995. **449**(1937): p. 669-677.

35. Lloyd, S., *Almost Any Quantum Logic Gate is Universal*. Physical Review Letters, 1995. **75**(2): p. 346.
36. Slichter, C.P., *Principles of Magnetic Resonance*. 3rd ed. 1990, New York: Spinger-Verlag.
37. Rouse, R., *Macroscopic Quantum Phenomena in an rf SQUID*, in *Physics*. 1996, State University of New York: Stony Brook.
38. Bayfield, J.E., *Quantum Evolution: An Introduction to Time-Independent Quantum Mechanics*, (Wiley and Sons, New York, 1999).
39. Fazio, R., G.M. Palma, and J. Siewert, *Fidelity and Leakage of Josephson Qubits.* Physical Review Letters, 1999. **83**(25): p. 5385.
40. Kouwenhoven, L.P., et al., *Observation of Photon-Assisted Tunneling through a Quantum Dot.* Physical Review Letters, 1994. **73**(25): p. 3443.
41. Nakamura, Y., Y.A. Pashkin, and J.S. Tsai, *Rabi Oscillations in a Josephson-Junction Charge Two-Level System.* Physical Review Letters, 2001. **87**(24): p. 246601.
42. Nakamura, Y. and J.S. Tsai, *A Coherent Two-Level System in a Superconducting Single-Electron Transistor Observed Through Photon-Assisted Cooper-Pair Tunneling.* Journal of Superconductivity, 1999. **12**(6): p. 799-806.
43. Oliver, W.D., et al., *Mach-Zehnder Interferometry in a Strongly Driven Superconducting Qubit.* Science, 2005. **310**(5754): p. 1653-1657.
44. Saito, S., et al., *Parametric Control of a Superconducting Flux Qubit.* Physical Review Letters, 2006. **96**(10): p. 107001.
45. Saito, S., et al., *Multiphoton Transitions in a Macroscopic Quantum Two-State System.* Physical Review Letters, 2004. **93**(3): p. 037001.
46. Amin, M.H.S., A.Y. Smirnov, and A. Maassen van den Brink, *Josephson-phase qubit without tunneling.* Physical Review B, 2003. **67**(10): p. 100508.
47. Zhongyuan, Z., I.C. Shih, and H. Siyuan, *Suppression of energy-relaxation-induced decoherence in Lambda-type three-level SQUID flux qubits: A dark-state approach.* Physical Review B (Condensed Matter and Materials Physics), 2004. **70**(9): p. 094513.
48. Zhou, Z., S.-I. Chu, and S. Han, *Quantum computing with superconducting devices: A three-level SQUID qubit.* Physical Review B, 2002. **66**(5): p. 054527.
49. Makhlin, Y., G. Schön, and A. Shnirman, *Quantum-state engineering with Josephson-junction devices.* Reviews of Modern Physics, 2001. **73**(2): p. 357.
50. Mooij, J.E., et al., *Josephson Persistent-Current Qubit.* Science, 1999. **285**(5430): p. 1036-1039.
51. John, M.M., et al., *Decoherence in Josephson Qubits from Dielectric Loss.* Physical Review Letters, 2005. **95**(21): p. 210503.
52. Berkley, A.J., et al., *Decoherence in a Josephson-junction qubit.* Physical Review B, 2003. **68**(6): p. 060502.

53. Itakura, T. and Y. Tokura, *Dephasing due to background charge fluctuations.* Physical Review B, 2003. **67**(19): p. 195320.
54. Roger, H.K., P.D. David, and C. John, *Model for 1/f Flux Noise in SQUIDs and Qubits.* Physical Review Letters, 2007. **98**(26): p. 267003.
55. Tian, L. and e. al., in *Quantum Mesoscopic Phenomena and Mesoscopic Devices in Microelectronics*: edited by Igor O. Kulik and R. Elliatioglu (Kluwer Academic, Dordrecht, 2000). p. 429.
56. Bialek, W., S. Chakravarty, and S. Kivelson, *Tunneling spectroscopy of a macroscopic variable.* Physical Review B, 1987. **35**(1): p. 120.
57. Schmidt, J.M., A.N. Cleland, and J. Clarke, *Resonant tunneling in small current-biased Josephson junctions.* Physical Review B, 1991. **43**(1): p. 229.
58. Chen, W., V. Patel, and J.E. Lukens, *Fabrication of high-quality Josephson junctions for quantum computation using a self-aligned process.* Microelectronic Engineering, 2004. **73-74**: p. 767-772.
59. Patel, V., et al., *A fast turn-around time process for fabrication of qubit circuits.* Applied Superconductivity, IEEE Transactions on, 2005. **15**(2): p. 117-120.
60. Han, S., J. Lapointe, and J. Lukens, *Activated Barrier Crossing*, G. Fleming and P. Hänggi, Editors. 1993, (World Scientific: Singapore ; River Edge, NJ). p. 241-267.
61. Li, S.-X., et al., *Quantitative Study of Macroscopic Quantum Tunneling in a dc SQUID: A System with Two Degrees of Freedom.* Physical Review Letters, 2002. **89**(9): p. 098301.
62. Lefevre-Seguin, V., et al., *Thermal activation of a hysteretic dc superconducting quantum interference device from its different zero-voltage states.* Physical Review B, 1992. **46**(9): p. 5507.
63. Tesche, C.D., *A thermal activation model for noise in the dc SQUID.* Journal of Low Temperature Physics, 1981. **44**(1): p. 119-147.
64. Zorin, A.B., *The thermocoax cable as the microwave frequency filter for single electron circuits.* Review of Scientific Instruments, 1995. **66**(8): p. 4296-4300.
65. Han, S., et al., *Time-Resolved Measurement of Dissipation-Induced Decoherence in a Josephson Junction.* Science, 2001. **293**(5534): p. 1457-1459.
66. Martinis, J.M., M.H. Devoret, and J. Clarke, *Experimental tests for the quantum behavior of a macroscopic degree of freedom: The phase difference across a Josephson junction.* Physical Review B, 1987. **35**(10): p. 4682.
67. Cryoengineering, G., *NbTi in CuNi wire*.
68. Harris, R., et al., *Sign- and Magnitude-Tunable Coupler for Superconducting Flux Qubits.* Physical Review Letters, 2007. **98**(17): p. 177001.
69. Nielsen, M.A. and I.L. Chuang, *Quantum Computation and Quantum Information*. 2000.

70. Yoshihara, F., et al., *Decoherence of Flux Qubits due to 1/f Flux Noise.* Physical Review Letters, 2006. **97**(16): p. 167001.
71. Yang, Y., et al., *Energy Relaxation Time between Macroscopic Quantum Levels in a Superconducting Persistent-Current Qubit.* Physical Review Letters, 2004. **92**(11): p. 117904.
72. Larkin, A.I. and N.O. Yu, *Effect of level quantization on the lifetime of metastable states.* Soviet Physics - JETP, 1986. **64**(1): p. 185-189.
73. Chiarello, F., *Quantum computing with superconducting quantum interference devices: a possible strategy.* Physics Letters A, 2000. **277**(4-5): p. 189-193.
74. Orlando, T.P., et al., *Superconducting persistent-current qubit.* Physical Review B, 1999. **60**(22): p. 15398.
75. Averin, D.V., *Adiabatic quantum computation with Cooper pairs.* Solid State Communications, 1998. **105**(10): p. 659-664.
76. Shnirman, A., G. Schön, and Z. Hermon, *Quantum Manipulations of Small Josephson Junctions.* Physical Review Letters, 1997. **79**(12): p. 2371.
77. Cirac, J.I. and P. Zoller, *Quantum Computations with Cold Trapped Ions.* Physical Review Letters, 1995. **74**(20): p. 4091.
78. Jones, J.A., M. Mosca, and R.H. Hansen, *Implementation of a quantum search algorithm on a quantum computer.* Nature, 1998. **393**(6683): p. 344-346.
79. Pellizzari, T., et al., *Decoherence, Continuous Observation, and Quantum Computing: A Cavity QED Model.* Physical Review Letters, 1995. **75**(21): p. 3788.
80. Pashkin, Y.A., et al., *Quantum oscillations in two coupled charge qubits.* Nature, 2003. **421**(6925): p. 823-826.
81. Martinis, J.M., et al., *Decoherence of a superconducting qubit due to bias noise.* Physical Review B, 2003. **67**(9): p. 094510.
82. Bertet, P., et al., *Dephasing of a Superconducting Qubit Induced by Photon Noise.* Physical Review Letters, 2005. **95**(25): p. 257002.
83. Bialczak, R.C., et al., *1/f Flux Noise in Josephson Phase Qubits.* cond-mat/0708.2125v1, 2007.
84. Sousa, R.d., *Dangleing-bond spin relaxation and magnetic 1/f noise from the amorphous-semiconductor/oxide interface: Theory.* cond-mat/0705.4088v2, 2007.
85. Kramers, H.A. and K.N.A. Wetenschap., *Proc. 33, 959 (1930).*
86. Abrahams, E., *Donor Electron Spin Relaxation in Silicon.* Physical Review, 1957. **107**(2): p. 491.
87. Averin, D.V., J.R. Friedman, and J.E. Lukens, *Macroscopic resonant tunneling of magnetic flux.* Physical Review B, 2000. **62**(17): p. 11802.
88. Il'ichev, E., et al., *Continuous Monitoring of Rabi Oscillations in a Josephson Flux Qubit.* Physical Review Letters, 2003. **91**(9): p. 097906.
89. Majer, J.B., et al., *Spectroscopy on Two Coupled Superconducting Flux Qubits.* Physical Review Letters, 2005. **94**(9): p. 090501.

Appendix A

Self Align Lift-off Process (SAL)

The qubit sample was fabricated on a 2" oxidized silicon wafer using the self-aligned lift-off (SAL) process for $Nb/AlO_x/Nb$ junctions. The process is shown in Chart 1. The $Nb/AlO_x/Nb$ trilayer is first patterned via lift-off. The lift-off has been used in order to minimize the number of reactive ion etches (RIE) of Nb. The process starts by coating a 50 mm diameter oxidized S_i wafer with a PMMA/P(MMA/MAA) bi-layer resist before exposure by deep ultraviolet (DVU) lithography and by electron beam lithography (EBL). Next, the $Nb/AlO_x/Nb$ trilayer is deposited via DC magnetron sputtering in the vacuum chamber with a Nb/Al dual-gun target. The bi-layer resist served as a lift-off mask for the base electrode layer. As the result, a 150 nm thick Nb layer has been formed to serve as the base electrode (BE) and counter electrode (CE) respectively. A 8-10 nm thick Al interlayer is also formed followed with thermal oxidation *in situ* to form the tunnel barrier after the BE deposition. The critical current density of the Josephson junctions is determined by the oxygen exposure (O_2 pressure $\times$ time) during the Al thermal oxidation. The base pressure of the sputtering chamber is around 10^{-7} Torr.

The junctions (CE) are patterned using a UVN-30 resist and exposed under DUV and EBL before developing for negative tone. A resolution of better than 100 nm can be achieved. The junctions are then defined by RIE of Nb (CE) in SF_6

plasma. Since the UVN-30 is not an etchable resist for SF_6 plasma, it forms an etch-stop mask for the junctions. As the Al interlayer also doesn't react with SF_6, it therefore serves as an end- point of the RIE when monitoring the Fluorine optical emission spectra during the etching process. Following the RIE, the wafer is RF sputtered with SiO_2 dielectrics, which served as an insulating layer between the BE and the wiring layer. The Nb (CE) is then exposed after the UVN-30 resist has been stripped and ready for the Nb wiring layer deposition.

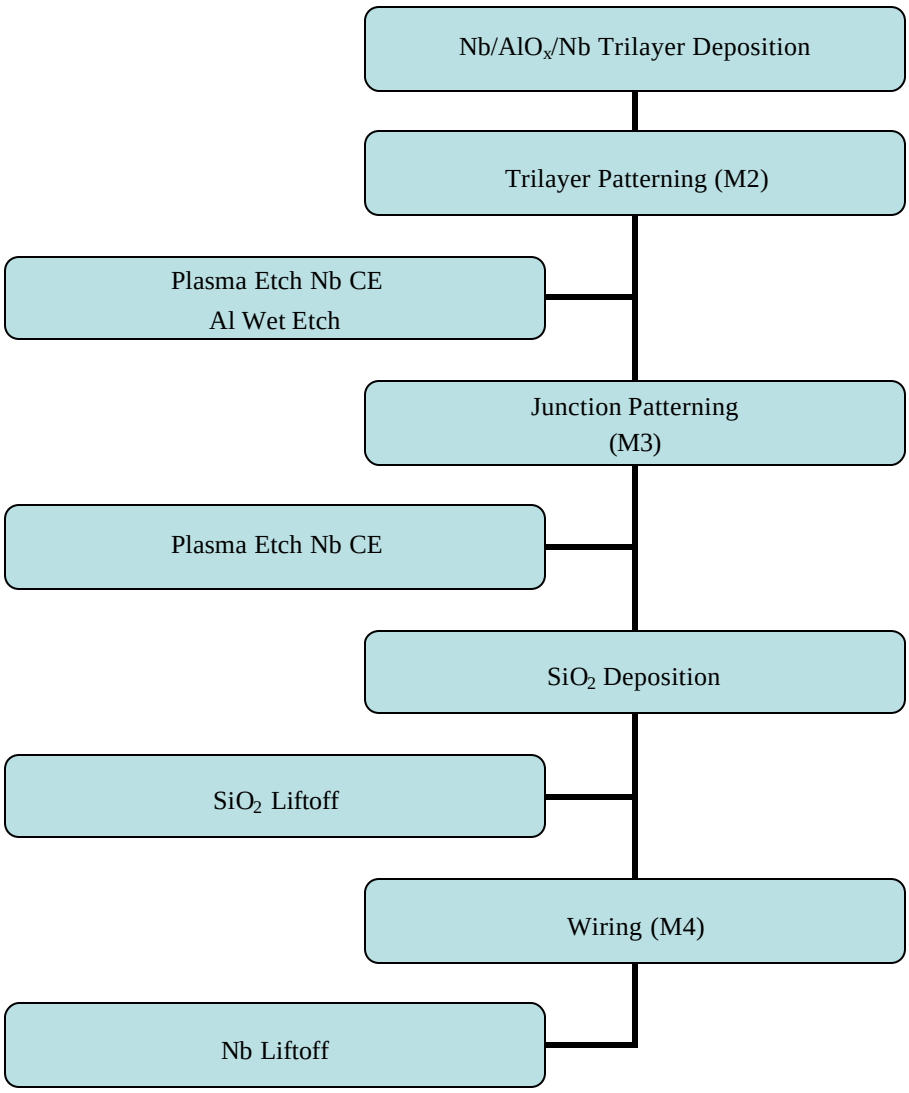

Chart 1. Schematic of the SUNY Nb/AlO$_x$/Nb junction fabrication process chart flow.

Appendix B

Dynamics of Λ-shaped three-level system

B.1 General Case

In the incoherent regime, all the possible transitions in a Λ-shaped three level system are depicted in Figure 3.6. The master equation of the system is the population rate equation which can be expressed as

$$\frac{dr_0}{dt} = g_{00} r_0 + g_{01} r_1 + g_{02} r_2, \tag{B.1a}$$

$$\frac{dr_1}{dt} = g_{10} r_0 + g_{11} r_1 + g_{12} r_2, \tag{B.1b}$$

$$\frac{dr_2}{dt} = g_{20} r_0 + g_{21} r_1 + g_{22} r_2, \tag{B.1c}$$

where, g_{ij} for $i, j = 0, 1, 2$ are the transition rates, whose values can be either positive or negative corresponding to the process of absorbing or emitting a photon. r_k for $k = 0, 1, 2$ are the populations in each energy level. For a population-conserved system, one has the following constrain:

$$r_0 + r_1 + r_2 \equiv 1 \tag{B.2}.$$

and thus

$$\frac{d(r_0 + r_1 + r_2)}{dt} = 0 \tag{B.3}.$$

By applying Equation (B.1a) to Equation (B.1c), then putting the result into Equation (B.3), the rates will satisfy

$$g_{00} + g_{10} + g_{20} = 0 \tag{B.4a}$$

$$g_{01} + g_{11} + g_{21} = 0 \tag{B.4b}$$

$$g_{02} + g_{12} + g_{22} = 0 \tag{B.4c}.$$

Let us assume r_0 and r_1 are the only two independent variables in Equation (B.3). The master equation can be reduced to

$$\frac{dr_0}{dt} = (g_{00} - g_{02})\, r_0 + (g_{01} - g_{02})\, r_1 + g_{02} \tag{B.5a},$$

$$\frac{dr_1}{dt} = (g_{10} - g_{12})\, r_0 + (g_{11} - g_{12})\, r_1 + g_{12} \tag{B.5b},$$

The general form of the population rate equation can be expressed by

$$\frac{dx_1}{dt} = a_{11}x_1 + a_{12}x_2 + c_1 \tag{B.6a},$$

$$\frac{dx_2}{dt} = a_{21}x_1 + a_{22}x_2 + c_2 \tag{B.6b},$$

where, x_1 and x_2 can be any two of r_1, r_2, and r_3 and a_{ij} and c_i $(i, j = 1,2)$ are the new constants related to the rate g_{ij} $(i, j = 1,2,3)$. For example, if $x_1 = r_0$ and $x_2 = r_1$, they are given by

$$\begin{cases} a_{11} = g_{00} - g_{02},\ a_{12} = g_{01} - g_{02}, \\ a_{21} = g_{10} - g_{12},\ a_{22} = g_{11} - g_{12}, \\ c_1 = g_{02},\ c_2 = g_{12}, \end{cases} \tag{B.7}.$$

The population rate equations given by Eq. (B.6a) and (B.7) can be rewritten in the matrix form

$$\frac{d\,r}{dt} = \mathbb{R}r + C \qquad \text{(B.8)},$$

where, r is the population density vector given by

$$r = \begin{pmatrix} x_1 \\ x_2 \end{pmatrix} \qquad \text{(B.9)}.$$

$\mathbb{R}$ is the rate matrix given by

$$\mathbb{R} = \begin{pmatrix} a_{11} & a_{12} \\ a_{21} & a_{22} \end{pmatrix} \qquad \text{(B.10)},$$

and C is the constant vector given by

$$C = \begin{pmatrix} c_1 \\ c_2 \end{pmatrix} \qquad \text{(B.11)}.$$

The exact solutions of the population rate equation are given by

$$\begin{aligned} x_1(t) = {} & A\frac{\left(a_{11} - a_{22} + \sqrt{T^2 - 4D}\right)}{2a_{21}}\exp\left[\frac{1}{2}\left(T + \sqrt{T^2 - 4D}\right)t\right] \\ & + B\frac{\left(a_{11} - a_{22} - \sqrt{T^2 - 4D}\right)}{2a_{21}}\exp\left[\frac{1}{2}\left(T - \sqrt{T^2 - 4D}\right)t\right] \\ & + \frac{c_2 a_{12} - c_1 a_{22}}{D} \end{aligned} \qquad \text{(B.12a)}$$

$$\begin{aligned} x_2(t) = {} & A\exp\left[\frac{1}{2}\left(T + \sqrt{T^2 - 4D}\right)t\right] + B\exp\left[\frac{1}{2}\left(T - \sqrt{T^2 - 4D}\right)t\right] \\ & - \frac{c_2 a_{11} - c_1 a_{21}}{D} \end{aligned} \qquad \text{(B.12b)},$$

where, T and D are the trace and determinant of the rate matrix $\mathbb{R}$ defined as $T = Trace(\mathbb{R}) = a_{11} + a_{22}$ and $D = \text{Determinant}(\mathbb{R}) = a_{11}a_{22} - a_{12}a_{21}$, respectively, and A and B are the constants dependent on the initial state given by

$$\begin{aligned} A &= (a + b) \\ B &= (a - b) \end{aligned} \tag{B.13},$$

with a and b defined by

$$\begin{aligned} a &= \frac{Dx_{20} + c_2 a_{11} - c_1 a_{21}}{2D} \\ b &= \frac{c_1 a_{21} T + (a_{22} - a_{11}) Dx_{20} + 2a_{21} Dx_{10} + c_2 (2D - Ta_{11})}{2D\sqrt{T^2 - 4D}} \end{aligned} \tag{B.14}.$$

Here, x_{10} and x_{20} are the initial values of x_{10} and x_{20} at time $t = 0$.

The solutions of Eq. (B.12) can be written in the form

$$x_i(t) = A_i \exp\left[\frac{1}{2}\left(T + \sqrt{T^2 - 4D}\right)t\right] + B_i \exp\left[\frac{1}{2}\left(T - \sqrt{T^2 - 4D}\right)t\right] + C_i \tag{B.15},$$

where, $A_i = a_i + b_i$, $B_i = a_i - b_i$ $(i = 1,2)$,

$$\begin{aligned} a_i &= \frac{1}{2D}\left[Dx_{i0} + c_i a_{jj} - c_j a_{ij}\right] \\ b_i &= \frac{1}{2D\sqrt{T^2 - 4D}}\left[c_j a_{ij} T + (a_{ii} - a_{jj}) Dx_{i0} + 2a_{ij} Dx_{j0} + c_i (2D - Ta_{jj})\right] \\ C_i &= \frac{c_j a_{ij} - c_i a_{jj}}{D} \end{aligned} \tag{B.16}$$

B.2 Special Case

For the special case described as the three-level system under the condition of microwave pumping and spontaneous decay process depicted in Figure 3.6. g_{02} is the

stimulated excitation (de-excitation) rate from $|0\rangle$ to $|2\rangle$, g_{21}, g_{20}, and g_{21} are the spontaneous decay rates from $|1\rangle$ to $|0\rangle$, from $|2\rangle$ to $|0\rangle$, and from $|2\rangle$ to $|1\rangle$ respectively. Let us redefine the total rate $g_t = g_1 + g_2$, where $g_1 = g_{02}$, $g_2 = g_{10}$, $g_3 = g_{20}$, $g_d = g_{21}$, and $\Gamma = g_1 + g_t + g_3 + g_d$. At time $t = 0$, $r_0 = 1$, and $r_1 = r_2 = 0$, thus $r_0 + r_1 + r_2 = 1$. The master equation (Eq. B.1) becomes

$$\begin{cases} \dfrac{dr_0}{dt} = -g_1 r_0 + g_t r_1 + g_3 r_2 \\ \dfrac{dr_1}{dt} = g_1 r_0 - g_t r_1 - g_d r_1 \\ \dfrac{dr_2}{dt} = g_d r_1 - g_2 r_2 \end{cases} \tag{B.17}$$

Put $\dfrac{dr_2}{dt} = 1 - \dfrac{dr_0}{dt} - \dfrac{dr_1}{dt}$ into Eq. (B.17) and one will get

$$\begin{aligned} \frac{dr_0}{dt} &= -(g_1 + g_3) r_0 + (g_t - g_3) r_1 + g_3 \\ \frac{dr_1}{dt} &= g_1 r_0 - (g_d + g_t) r_1 \end{aligned} \tag{B.18}.$$

Thus Eq. (B.7) becomes

$$\begin{cases} a_{11} = -g_1 - g_3, \; a_{12} = g_t - g_3, \\ a_{21} = g_1, \; a_{22} = -g_t - g_d, \\ c_1 = g_3, \; c_2 = 0, \end{cases} \tag{B.19}$$

Therefore, we will have

$$\begin{aligned} T &= a_{11} + a_{22} = -(g_1 + g_t + g_3 + g_d) = -\Gamma \\ D &= a_{11}a_{22} - a_{21}a_{12} = (g_1 + g_3)(g_t + g_d) - g_1(g_t - g_3) \\ 4D &= 4g_3(g_1 + g_d + g_t) + 4g_1 g_d \\ T^2 - 4D &= \left[(g_1 + g_d + g_t) - g_3\right]^2 - 4g_1 g_d = k^2(\Gamma - 2g_3)^2 \end{aligned}$$

where $k^2 = 1 - \frac{4g_1 g_d}{(\Gamma - 2g_3)^2}$. The solutions to the population rate equations are

$$\begin{aligned} x_1(t) &= A_1 \exp\left[\frac{1}{2}\left(T + \sqrt{T^2 - 4D}\right)t\right] + B_1 \exp\left[\frac{1}{2}\left(T - \sqrt{T^2 - 4D}\right)t\right] \\ x_2(t) &= A_2 \exp\left[\frac{1}{2}\left(T + \sqrt{T^2 - 4D}\right)t\right] + B_2 \exp\left[\frac{1}{2}\left(T - \sqrt{T^2 - 4D}\right)t\right] \end{aligned} \quad \text{(B.20)},$$

and

$$\begin{aligned} A_1 &= \frac{1}{2}\left[1 + \frac{g_t + g_d - g_1 - g_3}{k(\Gamma - 2g_3)}\right] r_{00} + \frac{g_t}{k(\Gamma - 2g_3)} r_{10} \\ B_1 &= \frac{1}{2}\left[1 - \frac{g_t + g_d - g_1 - g_3}{k(\Gamma - 2g_3)}\right] r_{00} - \frac{g_t}{k(\Gamma - 2g_3)} r_{10} \end{aligned} \quad \text{(B.21)}.$$

The two decay rates are

$$\begin{aligned} \Gamma_1 &= \frac{1}{2}\left[\Gamma - k(\Gamma - 2g_3)\right] \\ \Gamma_2 &= \frac{1}{2}\left[\Gamma + k(\Gamma - 2g_3)\right] \end{aligned} \quad \text{(B.22)}.$$

In general, for $A_1 > B_1$, if $T^2 - 4D \geq 0$, then the amplitude of the slow decay term (1st term) of Eq. (B.20) is larger than that of the fast decay term (2nd term) of Eq. (B.20). Therefore, only the 1st term will be left. The slow decay rate is

$$\begin{aligned} \Gamma_1 &= \frac{1}{2}\left\{\Gamma - \left[(2g_1 + g_2 + g_d - g_3)^2 - 4g_1 g_d\right]^{1/2}\right\} \\ &= \frac{1}{2}\left\{(g_1 + g_t + g_3 + g_d) - \left[(2g_1 + g_2 + g_d - g_3)^2 - 4g_1 g_d\right]^{1/2}\right\} \\ &= \frac{1}{2}\left\{(2g_1 + g_2 + g_3 + g_d) - \left[(2g_1 + g_2 + g_d - g_3)^2 - 4g_1 g_d\right]^{1/2}\right\} \end{aligned} \quad \text{(B.23)}$$

For weak microwave irradiation one has $g_1 = aP_{rf}$ according to Fermi's golden rule, where a is the coupling strength between the qubit and the applied microwave

and P_{rf} is the power of the applied microwave. The value of a can then be determined by measuring the relaxation rate as a function of P_{rf}.